Investigation of some metallic trilayer nickelates analogous to high T_c cuprates

A Thesis

submitted to
Indian Institute of Science Education and Research Pune
in partial fulfillment of the requirements for the
BS-MS Dual Degree Programme

by

Sanchayeta Ranajit Mudi

Indian Institute of Science Education and Research Pune
Dr. Homi Bhabha Road,
Pashan, Pune 411008, INDIA.

April, 2019

Supervisor: Dr.Surjeet Singh

Certificate

This is to certify that this dissertation entitled Investigation of some metallic trilayer nickelates analogous to high T_c cupratestowards the partial fulfilment of the BS-MS dual degree programme at the Indian Institute of Science Education and Research, Pune represents study/work carried out by Sanchayeta Ranajit Mudiat Indian Institute of Science Education and Research under the supervision of Dr.Surjeet Singh, Associate Professor, Department of Physics, during the academic year 2018-2019.

Dr.Surjeet Singh

Committee:

Dr.Surjeet Singh

Dr. Mukul Kabir

Declaration

I hereby declare that the matter embodied in the report entitled Investigation of some metallic trilayer nickelates analogous to high T_c cuprates are the results of the work carried out by me at the Department of Physics, Indian Institute of Science Education and Research, Pune, under the supervision of Dr.Surjeet Singh and the same has not been submitted elsewhere for any other degree.

Sanchayeta

Sanchayeta Ranajit Mudi

Acknowledgments

Firstly, I would like to thank my supervisor Dr. Surjeet Singh for giving me the opportunity to work on this project. His guidance and insight has helped structure this project. His faith in my abilities and constant motivation has immensely encouraged me. I will truly treasure all the fruitful discussions that I have had with him which have greatly enhanced my knowledge and understanding of the subject.

I would also like to thank members of Lab 210, h-cross block – Luminita ma'am, for the delicious cakes and cookies, Bag bhaiyya for motivational speeches and Bengali movie suggestions during late night chai at MDP, Prachi, Saurabh, Dibyata, Navita, Anupam, Haritha and Prakash for helping me out in the lab and for the daily dose of entertainment. I would specially like to thank Dibyata, who has been an integral part of this project and without whose help, this project and thesis would not have taken the shape that it has.

I would also like to thank the technical staff of h-cross block – Mr. Nilesh Dumbre and Mr. Sudhir Lone for resolving technical issues and Mr. Anil Prathamshetty and Mr. Yathish for FESEM Images and EDS. I would also like to thank the Government of India for providing me with the DST Inspire Scholarship during the course of my BS-MS education.

I am also grateful to my friends Namitha, Steenu, Surabhi and Mrutyunjay for the much needed pep talks, dinner outings and late night movies. And last, but not least, I would like to thank Maa and Baba who have been incredibly supportive through all these years and I would like to dedicate this thesis to them.

Abstract

The triple layer T′-structure compounds ($R_{n+1}Ni_nO_{2n+2}$ for n=3) have the mixed valent state of Ni^{1+}/Ni^{2+} which is analogous to the electronic configuration of Cu^{2+}/Cu^{3+} in the high temperature superconducting cuprates (HTSC). Hence such nickelates provide a fitting experimental platform to study their similarities as well as their differences with the HTSCs.

In this work, we tried to obtain the $R_4Ni_3O_8$ (R = La, Pr and Nd) compounds by subjecting the parent Ruddlesden Popper series members i.e. $R_4Ni_3O_{10}$ (R = La, Pr and Nd) to reducing conditions. The reducing conditions had to be precisely determined using the TGA setup. The $R_4Ni_3O_{10}$ members were synthesized by optimizing the sol-gel technique in which the citrate route was adopted. Structural, magnetic and electrical transport properties of $R_4Ni_3O_{10}$ samples were characterised. These low temperature physical property measurements revealed some new anomalies which were not reported earlier in the literature. In this thesis, we have attempted to gain insight into the origin of these anomalies.

Contents

List of Figures

List of Tables

Chapter 1

Introduction

Transition metal oxides (TMOs) exhibit a variety of exotic properties due to the strong electron correlations. Among the TMOs, the layered cuprates have garnered enormous attention due to the appearance of high temperature superconductivity(HTSC)[1]. These materials contain an underlying CuO_2 square lattice where the Cu ion is in square planar coordination with O ions.

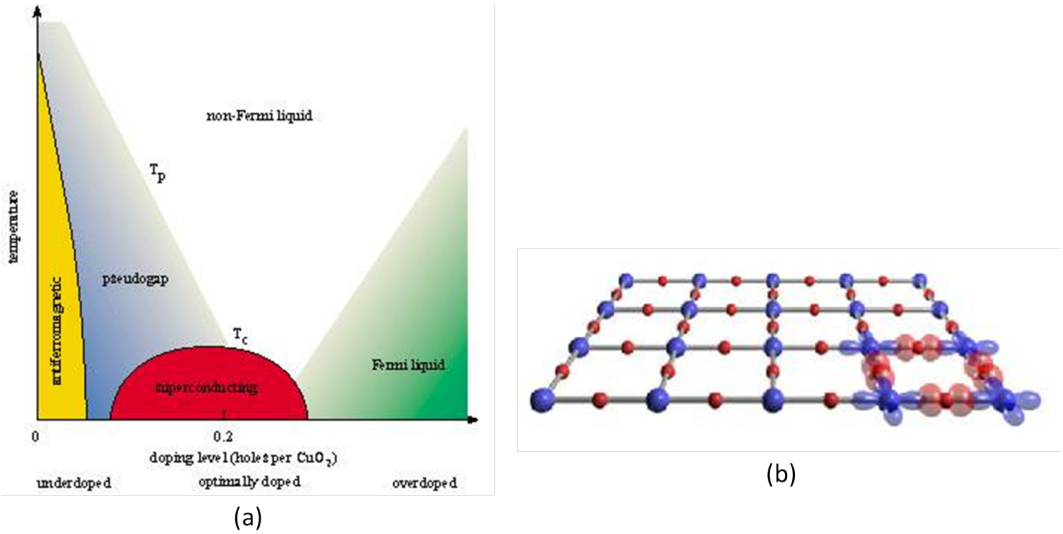

Figure 1.1: (a)Phase diagram of the cuprates (https://physicsworld.com/a/the-underdoped-phase-of-cuprate-superconductors) (b)Cu and O in square planar coordination in the CuO_2 plabe in the cuprates. The blue and red spheres represent Cu and O atoms respectively.

These materials are also characterized by a large orbital polarisation of the e_g states and the Fermi energy has $d_{x^2-y^2}$ character. Also, there is strong hybridisation between the O p and Cu d states. In the parent insulating samples, the Cu ions are in 2+ oxidation state (d^9 electronic configuration)- this results in a spin-1/2 system where the spins are antiferromagnetically aligned. Increasing the hole doping level helps to span the entire phase diagram of the cuprates. In the underdoped regime, below a critical temperature T_p, there is a decrease in the density of states at the Fermi energy which is known as the pseudogap state. On further increasing the doping level, superconductivity emerges at a critical concentration and temperature T_c . The T_c attains a maximum at an optimum doping level. On further increasing the doping level, at some critical doping concentration, superconductivity vanishes and the system moves into the Fermi liquid regime.

1.1 Structure

1.1.1 The Perovskite structure

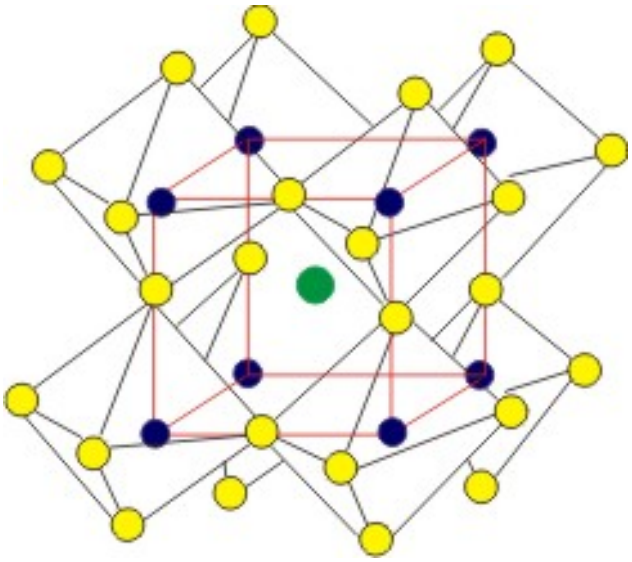

Figure 1.2: The perovskite structure. The green, blue and yellow spheres denote the A site cation, B site cation and X anions respectively.(https://nptel.ac.in/courses/113104005/lecture4/4_2.htm)

The perovskite structure has the general formula ABX_3, where A and B are cations with

the A cation being larger than the B cation and X is an anion. In the ideal cubic structure, the A cation sits at the corners of the cube and each A cation is surrounded by an octahedron of anions (i.e. A cation is in 6-fold coordination with the anions) while the B cation sits at the body-center and is in 12-fold coordination with the X anions. Slight changes in the radii of the cations causes distortion from the ideal cubic structure and this distortion can be described by the Goldschmidt tolerance factor t given by $t = \frac{(r_A + r_X)}{\sqrt{2}(r_B + r_X)}$ where r_A is the radius of the A site cation, r_X is the radius of the anion and r_B is the radius of the B site cation.The ideal value of t is 1 and as the value of t decreases, the distortion of the BO_6 octahedra increases and can lead to lowering of the symmetry (usually to orthorhombic or tetragonal) and coordination of the A and B cations.

Various layered structures such as the Aurivillius phase, the Dion-Jacobson phase and the Ruddlesden Popper phase can be derived from the perovskite structure. Here, we will focus on the Ruddlesden-Popper compounds.

1.1.2 Ruddlesden-Popper compounds

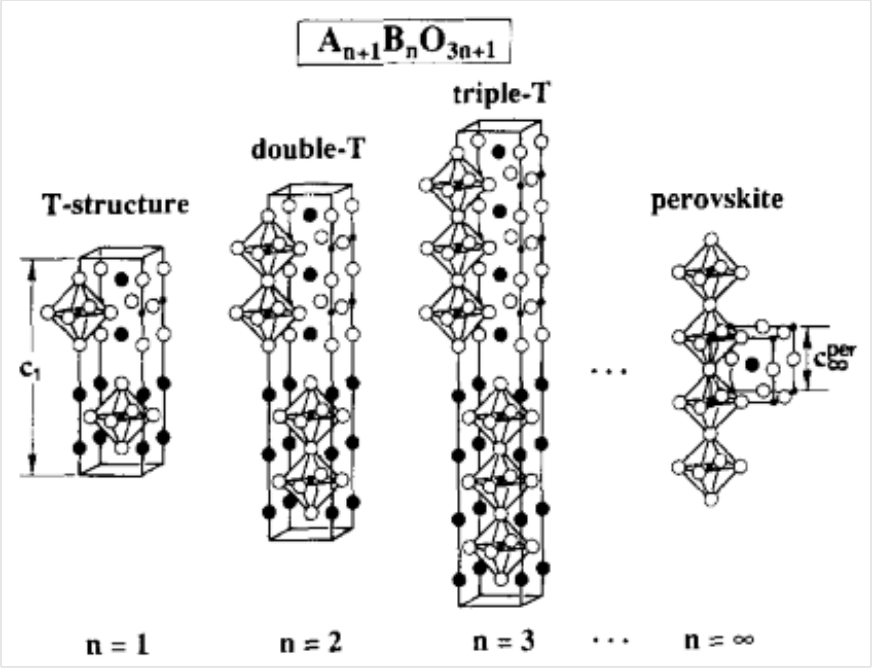

Figure 1.3: The n = 1, 2, 3 and ∞ members of the Ruddlesden-Popper compounds[2].

The Ruddlesden Popper (RP) phases with the T-structure can be described by the general formula $(AO)(ABO_3)_n$ or $A_{n+1}B_nO_{3n+1}$ where n ABO_3 perovskite layers are separated by a single AO rock-salt layer. In the case of nickelates which crystallize with the Ruddlesden-Popper structure, A is a rare earth ion R = La, Pr or Nd and B is nickel ion and therefore has the general formula $R_{n+1}Ni_nO_{3n+1}$.

For the n^{th} member of this series, n infinite perovskite $RNiO_3$ layers with corner sharing NiO octahedra in the ab plane are stacked along the c direction and each susch set of layers is separated from the other by a single RO rocksalt layer. The n=1, 2, 3 and ∞ members of this series is shown in Fig. 1.3. The average oxidation state of Ni is +2, +2.5, +2.67 and +3 for the n=1,2,3, and ∞ members respectively. As the number of perovskite layers increases, the conductivity of the sample also increases.

In this thesis, we will focus on the n=3 ($R_4Ni_3O_{10}$, henceforth abbreviated as R4310) member of this series. The Ni ions in this compound are in a mixed valent state with an average charge of +2.67 ($\frac{1}{3}$ Ni^{+2} and $\frac{2}{3}$ Ni^{+3}). As the size of the rare earth ion decreases, the Goldschmidt tolerance factor t also decreases. Since t $<$ 0.9 for these three R4310 compounds, they crystallize in the orthorhombic structure.

1.1.3 The T′-structure

Related to the Ruddlesden-Popper T-compounds are the T′-compounds which are obtained by reduction of the parent RP phases. They have the general formula $R_{n+1}Ni_nO_{2n+2}$, where R = La, Pr and Nd and n is the number of NiO square planes. Reduction causes deintercalation of the O ions from the perovskite layers in the RP phases and results in NiO square planes as depicted in Fig. 1.4. The nth member of this series contains n infinite NiO square planes connected via corner sharing in the ab plane stacked along the c direction. Each such set of planes is separated from the other by a single R_2O_2 fluorite layer. In this thesis, we will focus on the n=3 member of this series where Ni is in a mixed valent state with average charge of +1.33 ($\frac{2}{3}$ Ni^{1+} and $\frac{1}{3}$ Ni^{2+}).

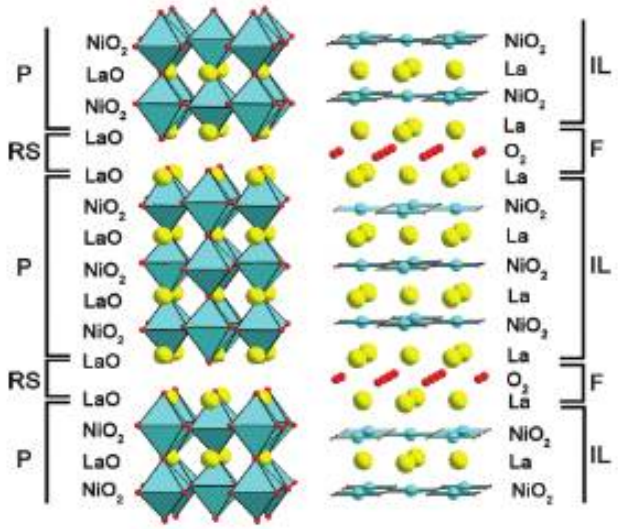

Figure 1.4: The n=3 member of the T′-structure from the corresponding Ruddlesden-Popper parent compound[3].

1.2 Motivation for studying layered nickelates

HTSCs have been studied for many decades now but the origin of this phenomenon in the cuprates is not very well understood. One of the approaches of studying the origin is to study materials with similar structural, electronic and magnetic properties as that of the cuprates. Nickelates are the most obvious place to look for these similarities since Ni and Cu are neighbours in the periodic table and some nickelates crystallize in structures similar to that of the cuprates. A theoretical prediction made by Anisimov et al [4] stated that Ni^{1+} in square planar coordination with O ions and doped with S=0 Ni^{2+} will host superconductivity. Compounds with the general formula $R_{n+1}Ni_nO_{2n+2}(R = La, Pr, Nd$ and n=3) (also known as the T'-structure) satisfy the condition given by Anisimov. X-ray absorption spectroscopy (XAS) measurements conducted on single crystals of $Pr_4Ni_3O_8$ by Zhang et al[5] revealed significant orbital polarisation of the e_g states with the unoccupied states above the Fermi energy showing $d_{x^2-y^2}$ orbital character, strong hydridisation of the O p and Ni d orbitals as well as low spin configuration of Ni^{2+}. While $La_4Ni_3O_8$ shows a semiconductor to insulator transition at 105 K that has been attributed to the onset of charge ordering in this system, $Pr_4Ni_3O_8$ remains metallic down to the lowest temperatures[5]. All these features shown by $Pr_4Ni_3O_8$, as discussed previously, are hallmarks of HTSC and

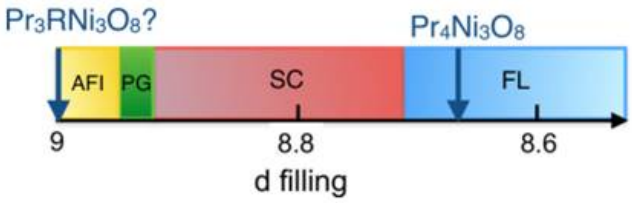

Figure 1.5: Position of $Pr_4Ni_3O_8$ in the phase diagram of the cuprates w.r.t the d electron count.

hence it will be interesting to study these systems. Also, recently, according to another theoretical paper[6], doping a 4+ cation like Ce at the Pr site in $Pr_4Ni_3O_8$ at an optimal doping concentration of $\sim 1/8$ will help in electron doping the system and moving it from the Fermi liquid regime into the superconducting regime with respect to the d-electron count (Fig. 1.5).

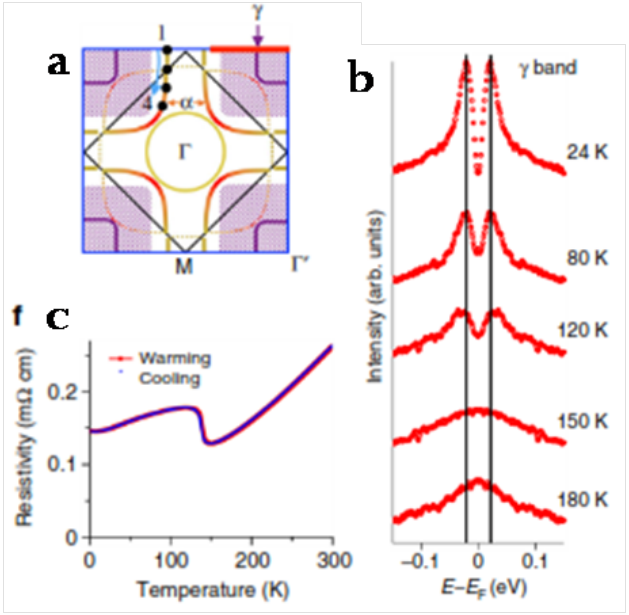

Figure 1.6: (a) Fermi surface of $La_4Ni_3O_{10}$ at 30 K, (b)The gap evolution of the γ band with temperature which coincides with the resistivity anomaly. Figures taken from reference [7].

To obtain the T'-compounds, we will need to reduce the parent Ruddlesden Popper (RP) compounds with the T-structure. The parent RP phases are interesting in themselves and their low temperature properties are not very well understood/studied. The n=3 member of

this family shows a metal-to-metal transition at 138.6 K ($La_4Ni_3O_{10}$), 145 K ($Pr_4Ni_3O_{10}$) and 165 K ($Nd_4Ni_3O_{10}$)[8]. The main point that motivated us to study this series is the fact that there is very less understanding of the origin of the resistivity anomaly and whether charge density wave (CDW) instability is the reason behind this phenomenon is still under speculation. Recently, ARPES measurements[7] on single crystals of $La_4Ni_3O_{10}$ done by Li et al revealed similarities and differences between the low-energy electronic structure of layered cuprates and that of $La_4Ni_3O_{10}$. They observed an extra $d_{3z^2-r^2}$ band which exhibits a gap opening between 120 K and 150 K. The concomitant appearance of the gap evolution and the resistivity anomaly (Fig. 1.6) has been attributed to a possible CDW ordering in this system though this has not been experimentally confirmed yet. Another recent theoretical paper[9] suggested that the appearance of the gap in $La_4Ni_3O_{10}$ could be due to a structural transition from an orthorhombic Bmab phase at room temperature to a monoclinic $P2_1/a$ phase below the transition and that this structural transition is not necessarily driven by a CDW instability in this system.

In the present work, we have made an attempt to gain insight into the low temperature properties of the $R_4Ni_3O_{10}$ and $R_4Ni_3O_8$ series. Sol-gel technique, rather than the traditional solid-state route, was used to synthesize the $R_4Ni_3O_{10}$ compounds. An attempt was also made to synthesize the Ce-doped compound using this technique. These compounds were then reduced to obtain the $R_4Ni_3O_8$ compounds. Thermogravimetric Analysis was used to determine the precise conditions for this reduction. A detailed study of the structural characterisation and low temperature properties of these compounds has been made. New features have been observed in the resistivity, magnetisation and specific heat data which have not been observed previously. An attempt has been made to interpret these anomalies in the results and discussion section of this thesis.

Chapter 2

Experimental Techniques

2.1 Thermogravimetric Analysis (TGA) :

The R438 samples cannot be directly synthesized in lab. To obtain the R438 phase, one needs to reduce the parent R4310 compounds. The conditions for this reduction are not well reported in the literature and hence we performed TGA measurements on the R4310 samples to ascertain the temperature and time range for which the R438 samples are stable.

Thermogravimetric Analysis (TGA) is a technique which is used to probe the change in mass of a sample as a function of temperature or time. Various processes can lead to a change in sample mass such as –

- Oxidation of metals in air or oxygen
- Loss of water of crystallization or uptake of moisture by the sample
- Reduction of the sample in the presence of a reducing gas such as H_2 and subsequent evolution of gases
- Thermal decomposition of samples in an inert atmosphere leading to formation of volatile products
- Oxidative decomposition of organic substances in air or oxygen

- Ferromagnetic material, for which the change in magnetisation of the sample at the Curie temperature generates a TGA signal.

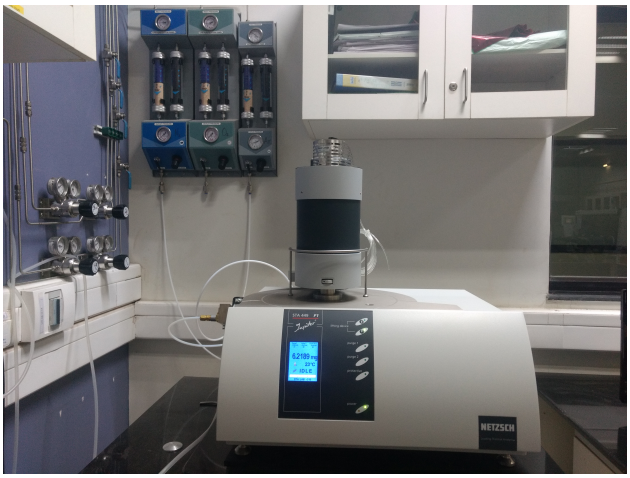

Figure 2.1: TGA setup

To accurately monitor the temperature of the sample, a thermocouple, which is a temperature sensor, is used. The choice of thermocouple depends on the atmosphere that will be used during the experiment and the temperature range for which it will be used. The information is summarized in the table given below :

Table 2.1: Thermocouple details

Thermocouple	Temperature range	Atmosphere
Type E (Chromel-Konstantan)	-150^oC to 700^oC	oxidizing and inert; limited use in vacuum or reducing
Type K (Chromel-Alumel)	-150^oC to 800^oC	Clean oxidizing and inert; limited use in vacuum or reducing
Type S (Pt-10%Rh/Pt)	RT to 1650^oC	oxidizing and inert
Type B (Pt-30%Rh/Pt-6%Rh)	RT to 1700^oC	oxidizing and inert
Type P (Platinel)	-150^oC to 1000^oC	oxidizing and inert
Type W (W3%Re-W25%Re)	RT to 2400^oC	inert, reducing and vacuum; not for use in oxidizing atmosphere

Two kinds of measurements were carried out on the R4310 samples – dynamic mea-

surement where the sample was heated at a constant rate to ascertain the temperature at which the required transitions happen followed by isothermal measurements at various temperatures to obtain the duration for which the R438 phase is stable. The experiments were carried out in a Netzsch STA 449 F1in TG mode with a silicon carbide furnace ($25-1600^oC$) and alumina crucible (3.5 mL) in an Ar (90%) - H_2 (10%) atmosphere. Since we have used a reducing atmosphere, W (W3%Re-W25%Re) type thermocouple was used. A flow rate of 10 mL/min for $Ar - H_2$ through the sample chamber and 20 mL/min for N_2 through the balance chamber was maintained during all the experiments. To facilitate the reaction, all the samples were loaded in powder form. For all the R4310 samples, initially, a heating rate of 10 K/min was employed for the temperature scan from 20^oC to 700^oC. Lower heating rates of 5 K/min and 2.5 K/min were also used to better resolve certain steps in the TGA plots. Baseline corrections were subtracted from the sample measurement curves to eliminate instrumental errors and to correct for buoyancy.

2.2 Synthesis

It had been previously reported[10] that the solid state synthesis of the R4310 compounds yield a mixture of phases even after several sinterings. Hence we have employed the citrate method to obtain pure phases of the R4310 compounds. The advantage of this method is that precursors with small particle size are obtained – this increases the surface area available for reaction.

The precursors used for the synthesis of R4310 compounds were La_2O_3 (Sigma Aldrich, 99.99%), Pr_6O_{11} (Sigma Aldrich, 99.99%), Nd_2O_3 (Sigma Aldrich, 99.99%) and NiO (Sigma Aldrich, 99.999%).The following reaction equations were used for estimating the amount of precursors required for preparing 3 g of the sample :

$$2La_2O_3 + 3NiO + \tfrac{1}{2}\ O_2 \rightarrow La_4Ni_3O_{10}$$
$$2Pr_6O_{11} + 9NiO \rightarrow 3Pr_4Ni_3O_{10} + \tfrac{1}{2}\ O_2$$
$$2Nd_2O_3 + 3NiO + \tfrac{1}{2}\ O_2 \rightarrow Nd_4Ni_3O_{10}$$

The rare earth oxides were put for pre-heating at 1000^oC before stoichiometric amounts of these precursors were weighed out at 200^oC. To this, stoichiometric amount of NiO was added. The precursors were finely ground together and then put in a beaker containing a

solution of 80 mL Millipore water and 20 mL HNO_3 (70%w/w, Thomas Baker) at 100^oC with constant stirring using a magnetic stirrer. The solution was dark green. An equivalent

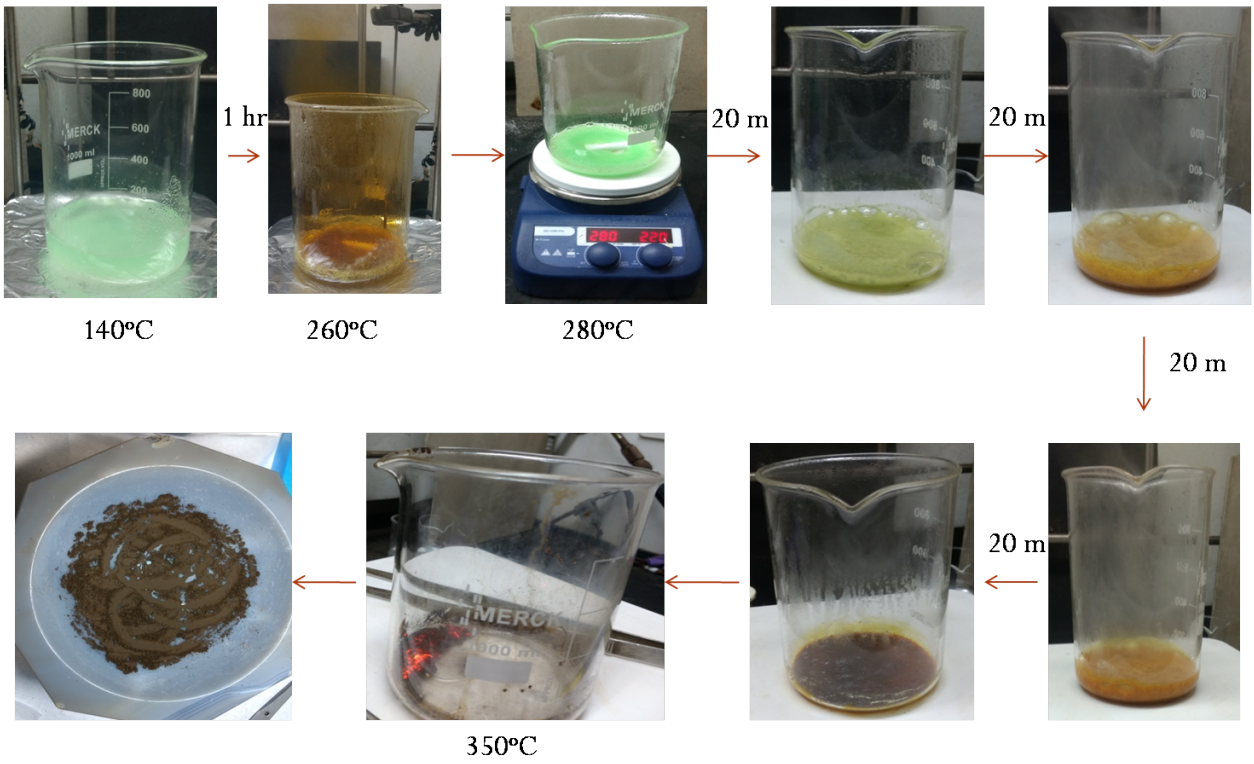

Figure 2.2: Synthesis procedure

molar proportion of citric acid w.r.t the precursors was added (∼60 g of citric acid was used for synthesizing 3 g of sample). We found that the precursors did not dissolve in the solution. So more HNO_3 was added till all the powder dissolved and the solution turned light green. Then the temperature was slowly increased from 100^oC to 280^oC. During this time, the reddish brown vapours of nitric acid evaporated and the solution attained a gel-like texture. Thereafter, the temperature was slowly increased from 280^oC to 350^oC. During this time, the gel turned from light green to yellow to brown while drying up. At 350^oC, the dried powder auto-ignited and a grey powder was obtained. The grey powder was collected from the beaker and ground thoroughly before sintering it in a tube furnace. Each sintering (except the 1st one) was carried out in pellet form for 24 hours.

The Goldshmidt tolerance factor t (discussed in section 1.1.1) influences the distortion of the crystal, which in turn influences the temperature at which the samples should be

sintered. As the radius of the lanthanide ion R decreases, the temperature at which the corresponding R4310 phase is stabilized decreases.The sinterings were carried out at 1100^oC for La4310, 1050^oC for Pr4310 and 1000^oC for Nd4310.

Since one of the objectives of this research proposal was to synthesize $Pr_4Ni_3O_8$ with Ce doping at the Pr site, we tried to synthesize Ce doped $Pr_4Ni_3O_{10}$ followed by reduction to get the corresponding T'-phase. Synthesis of $Pr_{3.8}Ce_{0.2}Ni_3O_{10}$ (Pr4310 with 5 % Ce doping at the Pr site) was tried using the citrate method (∼60 g of citric acid was used for synthesizing 1 g of the sample). Sinterings were performed at 1050^oC under flowing O_2 atmosphere.

2.3 Sample Characterization

2.3.1 XRD Analysis

Powder x-ray diffraction is a powerful tool used for characterizing crystalline samples. Crystals, on account of the presence of periodic arrangement of atoms, act as a diffraction grating and diffract x-rays that are incident on them (since the wavelength of x-rays is comparable to the spacings between the crystal planes).

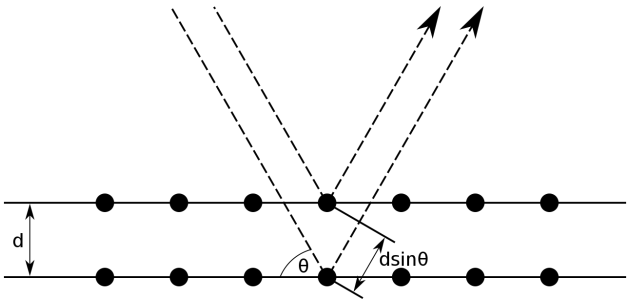

Figure 2.3: Bragg reflection (Source : Wikipedia)

Constructive interference of the scattered rays satisfy Bragg's condition given by:

$$2d \sin\theta = n\lambda$$

where, d is the spacing between the crystallographic planes, θ is the angle that the incident ray makes with the crystal plane and λ is the wavelength of the incident x-ray. Each crystalline material has a unique diffraction pattern that can be used for its characterization. The diffraction pattern can also be used for obtaining cell parameters.

Powder x-ray diffraction was carried out on all sintered samples for confirming purity of the desired phase using Bruker D8 Advance powder X-Ray diffractometer (Cu K alpha radiation with $\lambda = 1.5406$ Å). For determining cell parameters, the samples were ground thoroughly and some Si powder was mixed with it (Si is used as an internal standard). Oil was then smeared on a glass slide and the powder was sprinkled on it. Extra powder was tapped off before taking the scans.

2.3.2 FESEM and EDAX

Field Emission Scanning Electron Microscope (FESEM) is a characterization technique that can be used for imaging sample surfaces. An electron beam emanating from a cathode is accelerated by a potential gradient (of the order of kV) and is focused using electromagnetic and electrostatic lenses. When the primary electrons (PE) of the beam interact with the sample, secondary electrons (SE) and back scattered electrons (BSE) are released and their energy contains information about the sample topology. SE are emitted by interaction of the PE with the outer atomic shell of the material whereas BSE are emitted due to scattering processes that take place much deeper inside the sample. SE are detected by an in-lens detector that carry information about the sample surface while BSE are detected by an AsB detector and can be used for determining both sample topography and compositional differences (due to the changes in contrast).

Energy Dispersive X-ray Spectroscopy (EDS) is a technique which is often used along with FESEM for sample characterization. It is used for estimating elemental composition of the sample. In this method, a beam of electrons is made incident on the sample. The beam knocks out an electron from one of the inner shells of the atom. This creates a hole in the shell which is then occupied by an electron from a higher energy level; this leads to emission of x-rays which are characteristic of the element. For $Z < 11$, since the outer atomic shell is involved in bonding, the chemical environment influences the energy level spacings and therefore the characteristic x-rays which are used to identify the element. Hence, with this

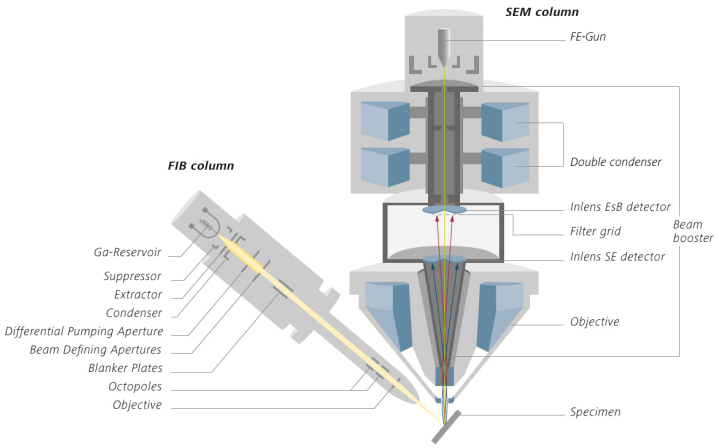

Figure 2.4: Schematic of FESEM instrument (https://www.zeiss.com/microscopy/int/products/fib-sem-instruments/crossbeam/crossbeam-technology.html)

technique, accurate readings are obtained for Z > 11.

Zeiss Ultra Plus was used for obtaining FESEM and EDS on our samples. Tiny pieces of our samples with polished surfaces were stuck on a double sides carbon tape and loaded onto the sample puck. Images were taken at 15 kV, 18 kV and 20 kV.

2.3.3 Measurement of Physical Properties :

The variation of physical properties like resistivity, susceptibility, thermopower and heat capacity with temperature (2 K to 300 K) was probed using a Quantum Design Physical Properties Measurement System (QD PPMS).

2.3.4 Transport measurements

2.3.5 Resistivity

The resistance of a material is a measure of the amount of obstruction it offers to the flow of current. While the resistance of the material depends on the size and shape of the sample,

resistivity is a characteristic of the material and is given by :

$$\rho = \frac{RA}{l} = \frac{VA}{Il}$$

where R is the resistance, V is the voltage difference across the sample, I is the current flowing through the sample, A is the cross-sectional perpendicular to the current flow and l is the distance between the voltage probes.

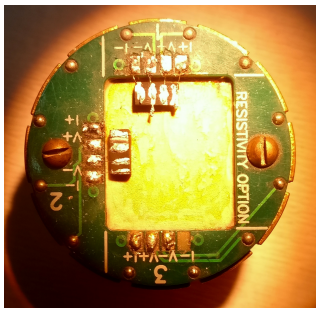

Figure 2.5: Samples mounted on a DC resistivity puck

For carrying out these measurements, a cigarette paper was stuck to the puck using GE varnish. This provides electrical insulation between the puck and the sample and rectangular pieces of the samples were mounted on the resistivity puck. Since the surface of the puck is conducting, before loading the sample, a cigarette paper was stuck to the puck using GE varnish. This provides electrical insulation between the puck and the sample. Four probe measurements were done on all the samples. One end each of four gold wires were soldered onto the user bridge and the other end was used to make line contacts on the sample using silver paint. Data was collected but during heating and cooling cycles. Magnetic field dependent measurements were also done (at 5 T).

2.3.6 Thermopower

The thermal transport option (TTO) of the QD PPMS can be used to measure the the thermal conductivityκ, the Seebeck coefficient (or thermopower) α and the electrical resistivity ρ of a material. By passing a square heat pulse and measuring the temperature gradient across the sample, the thermal conductivity can be calculated if the sample dimensions are

known. The Seebeck coefficient is obtained by measuring the voltage drop ΔV across the sample due to the temperature gradient δT. The resistivity is measured in accordance with the AC transport option of the PPMS. These three quantities can be used to compute a value called the thermoelectric figure of merit ZT which is defined as $ZT = \frac{\alpha^2 T}{\kappa\rho}$, and its value is a measure of the suitability of the material for thermoelectric applications ($ZT > 1$ is used as a benchmark).

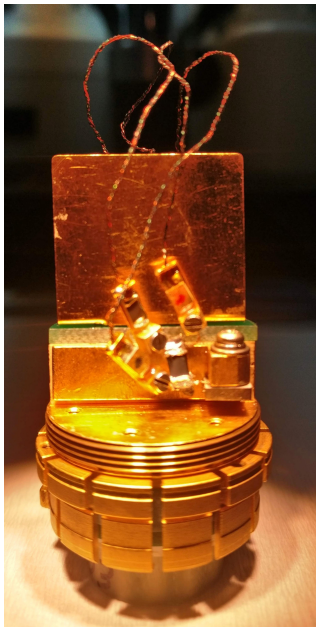

Figure 2.6: Sample mounted on Thermopower setup

Four leads are required for the measurements of κ, α and ρ – a heater (which is also the current source I+ for resistivity measurements), a hot thermometer (also used as V+), a cold thermometer (also used as V-) and a cold foot (used as I-). These measurements can be done using either the four probe measurement or the two probe measurement technique. Two probe measurements should be done only when the thermal and electrical resistance of the leads is very low compared to that of the sample.

For measuring κ, α and ρ of our samples, we did two probe measurements. Copper wires were tightly wound around the ends of a rectangular bar of the sample and a generous amount of silver paint was applied to make good thermal and electrical contact between the sample and the leads. The leads are then connected to the heater and thermometer shoes and attached to the sample puck as shown in the Fig. 2.6. A radiation shield is then used

to cover the puck so that radiation between the sample and the environment is minimized. The measurements were carried in continuous mode in which the system continuously adjusts parameters like the heater power and period to optimize the measurements. Also, these measurements are carried out in high vacuum so that heat loss to the environment is minimized.

2.3.7 Magnetic Measurements

Magnetic measurements (magnetisation M) were performed using the Vibrating Sample Magnetometer (VSM) option of the PPMS. M vs T measurements were done under a constant magnetic field H (=1000 Oe, 5000 Oe and 1 T) whereas M vs H measurements were done at a constant temperature T (= 5 K). The working principle of VSM is based on Faraday's

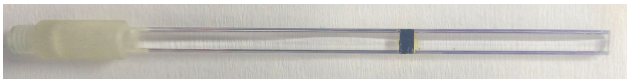

Figure 2.7: Sample mounted on quartz VSM sample holder

Law. In this technique, a sample is mounted on a quartz sample holder which vibrates linearly inside a coil. According to Faraday's law, when the magnetic flux through a coil changes with time, it induces a voltage in it. This voltage is proportional to the frequency of oscillation of the rod, amplitude of oscillation and the magnetic moment of the sample.

2.3.8 Heat Capacity

The heat capacity option of the PPMS was used for measuring heat capacity at constant pressure Cp i.e. $Cp = \frac{dQ}{dT}_p$. Since electrons and phonons are carriers of heat, changes in the crystal or magnetic structure affect the heat capacity of the sample and are reflected in such measurements.

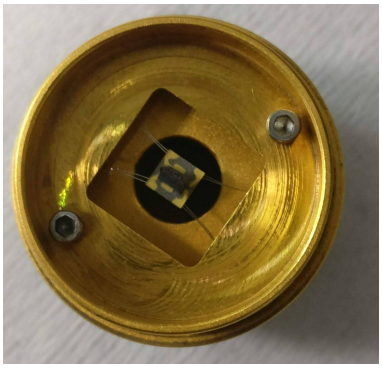

Figure 2.8: Sample mounted on heat capacity sample holder

For performing these measurements, sample is loaded onto the puck using N grease. This gives the total heat capacity of the sample, grease and the puck. The heat capacity of the sample is obtained by subtracting the addenda (which is a measure of the heat capacity of the sample and the puck) from the total heat capacity. Field dependent measurements were also performed at 1 T, 3 T and 5 T.

Chapter 3

Structural Characterization

In Chapter 2, a detailed account of the method that was used for synthesizing the R4310 samples and a basic introduction to characterization techniques like x-ray diffraction, FE-SEM and EDS were given. This chapter deals with the results of these characterization techniques – x-ray patterns obtained after each sintering for all the samples were compared with the simulated patterns of the final products to monitor the progress of the reaction. Wherever required, changes were made in the synthesis conditions to obtain the desired product. FESEM and EDS was also done on the final sintered pellets to determine the homogeneity of the samples and to determine the elemental composition.

3.1 XRD Analysis

XRD was done after each sintering on all the samples to monitor the progress of the reaction. Although carrying out 3 sinterings is sufficient for obtaining a pure phase, we carried out nearly 7 sinterings for each sample because changes in the intensity of certain peaks were observed during the X-ray analysis.

It had been previously reported[8] that sintering for La4310 can be performed in air at 1100^oC whereas sintering for Pr4310 and Nd4310 samples should be performed under flowing O_2 atmosphere at 1050^oC and 1000^oC respectively. But, in the case of La4310, after 4th sintering in air, it was observed that peaks corresponding to La327 phase were also present.

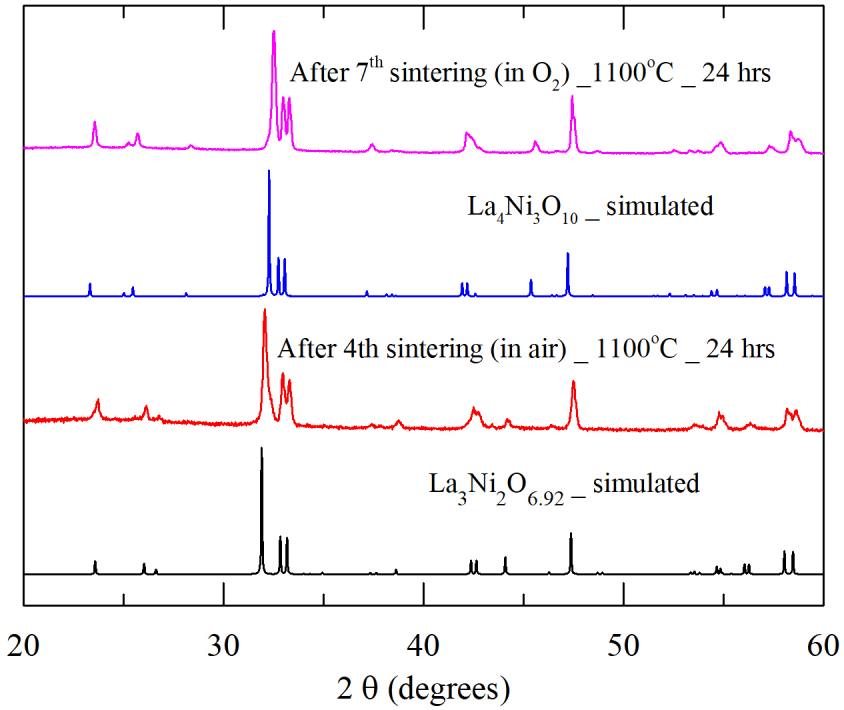

Figure 3.1: XRD pattern of La4310 after 4^{th} and 7^{th} sintering

Hence, we switched to O_2 atmosphere. Comparison of the XRD plot after 3 sinterings of these pellets in O_2 atmosphere with the simulated pattern of La4310 confirmed the purity of this phase Fig.3.1.

Also, for the R4310 samples, the possibility of intergrowths of two or more members of the $R_{n+1}Ni_nO_{3n+1}$ series cannot be ruled out. Hence, we have compared the XRD of our samples with the patterns for R214 and R113 members also. As can be seen from Fig. 3.2 and 3.3, the XRD pattern of our samples show a good match with the simulated pattern for R4310 while peaks of the R214 and R113 phases are either absent or present below the detection limit of the XRD technique, thereby confirming the purity of our samples.

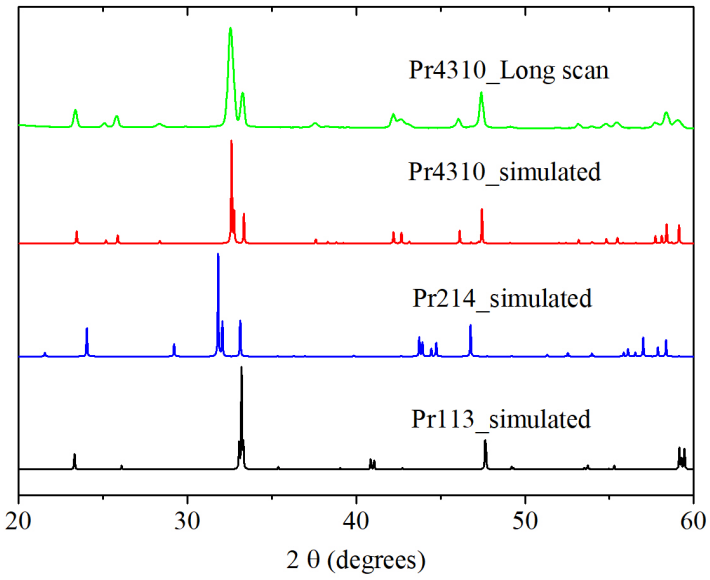

Figure 3.2: Comparison of XRD pattern of Pr4310 after 7^{th} sintering with simulated patterns for Pr4310, Pr113 and Pr214

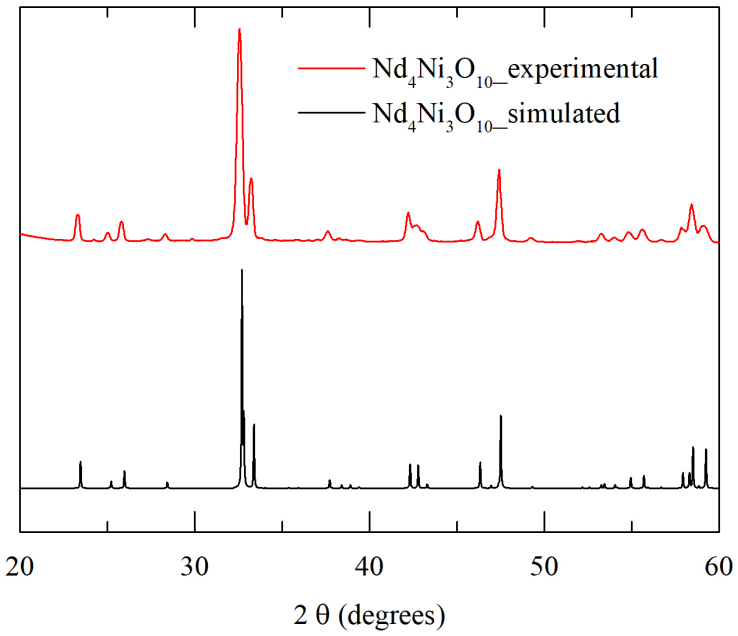

Figure 3.3: Comparison of XRD pattern of Nd4310 after 7^{th} sintering with its simulated pattern.

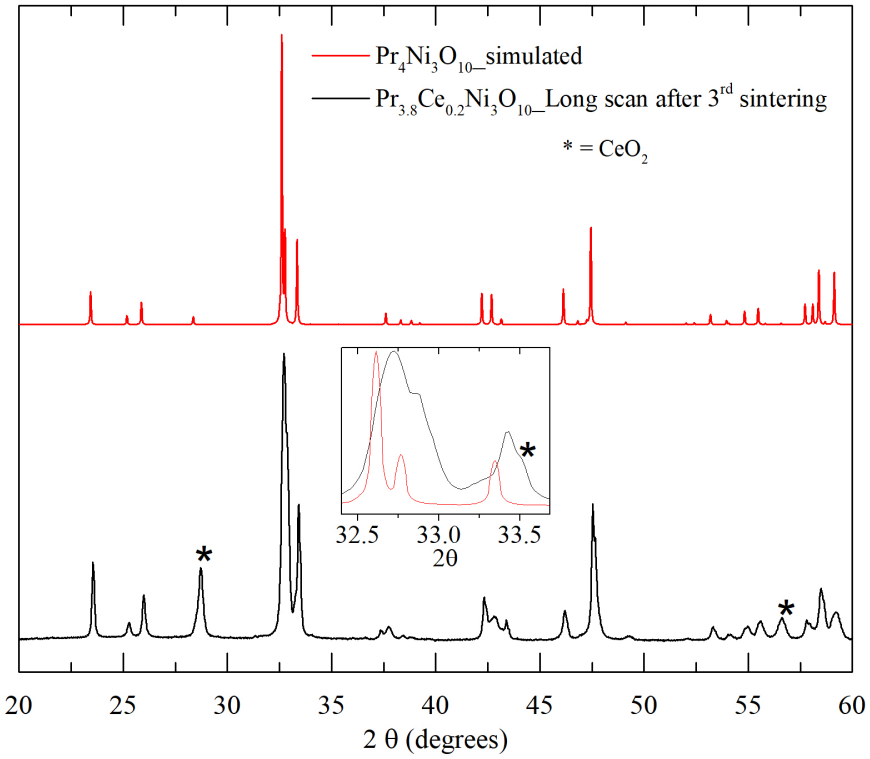

Figure 3.4: Comparison of XRD pattern of Ce-doped Pr4310 after 3^{rd} sintering with simulated pattern of Pr4310. Inset shows peaks of CeO_2.

XRD analysis of the $Pr_{3.8}Ce_{0.2}Ni_3O_{10}$ sample after 3rd sintering showed large, unreacted CeO_2 peaks (marked with an asterisk in Fig. 3.4) which suggests that Ce does not substitute Pr in Pr4310. But a small shift in the XRD pattern to higher angles suggest that a small amount of Ce^{4+} may have replaced Pr^{3+}. However, due to the presence of substantial quantity of unreacted CeO_2, we did not investigate this sample any further.

We also calculated the a, b and c parameters for our samples using UnitCell[11] software. They are summarized in table 3.1. As expected, the cell parameters and the unit cell volume decrease as the size of the rare earth ion decreases.

Table 3.1: Cell parameters for the R4310 compounds

Compound	a (Å)	b (Å)	c (Å)	V (Å^3)
La4310	5.38406	5.48105	27.76415	819.3284
Pr4310	5.37028	5.46247	27.51095	807.0337
Nd4310	5.35591	5.45676	27.37141	799.9559

We have also successfully reduced the R4310 samples to the R438 phases for R= Pr and Nd. XRD of the final product shows a good match with the simulated patterns of these phases as shown in Fig. 3.5. Cell parameters, calculated using UnitCell software, are summarized in table 3.2. As expected, the cell parameters decrease with decreasing size of the lanthanide ion.

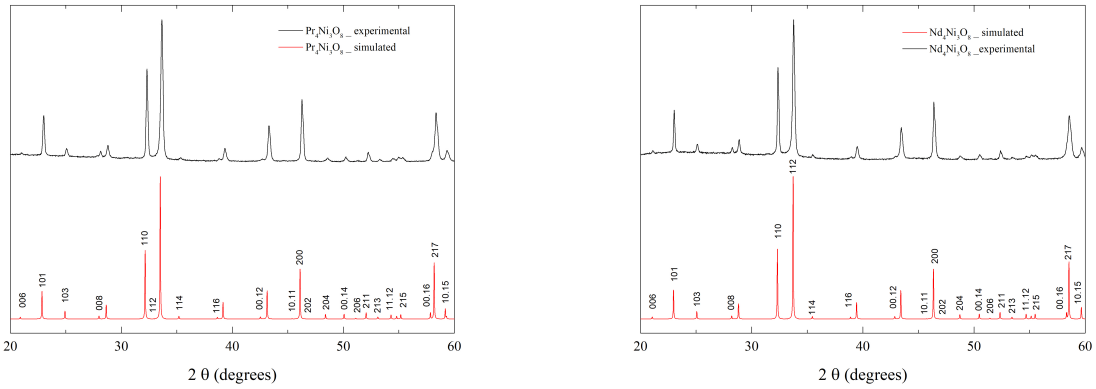

Figure 3.5: Comparison of XRD patterns of Pr438 and Nd438 with their respective simulated patterns.

Table 3.2: Cell parameters for the R438 compounds

Compound	a (Å)	c (Å)	V (Å^3)
Pr438	3.93037	25.33170	391.3185
Nd438	3.92831	25.21465	389.1035

3.2 FESEM and EDS

FESEM images of all the R4310 samples were obtained at 20 kV. EDS spectra were obtained at 9 points for each sample. The R:Ni ratio was calculated for each spectrum and then averaged. The average R:Ni ratio was 1.45, 1.38 and 1.42 for R = La, Pr and Nd respectively. These values are slightly higher than the theoretical value of 1.33 for these samples, especially for the La sample. For the La sample, the La:Ni ratio is closer to that expected for La327. However, from Fig.3.1, after the final sintering, La327 is not present in the sample. Hence, these higher values could be due to higher error bars of EDS. The grain size and shape are similar for all three samples and hence, the effect on the resistivity due to grain boundaries will be similar for all three samples.

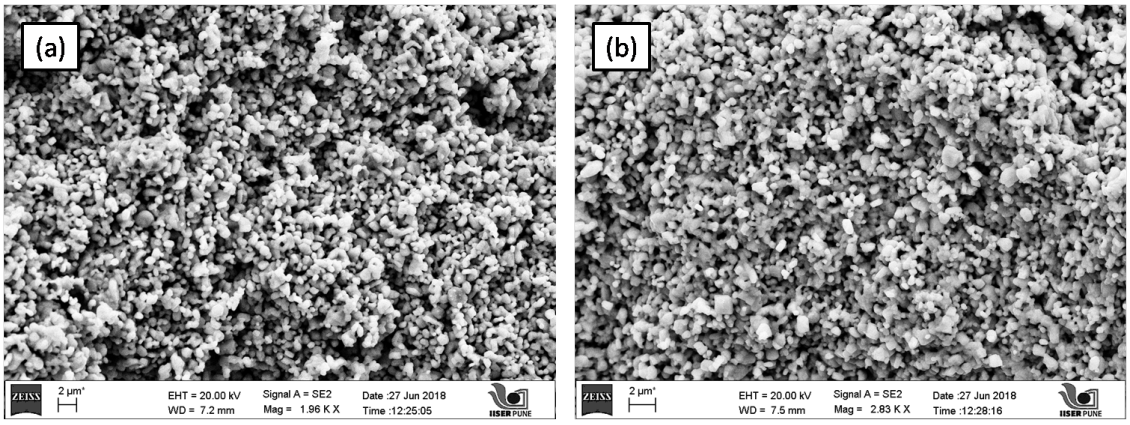

Figure 3.6: FESEM images at 20 kV for (a)Pr4310 and (b)Nd4310.

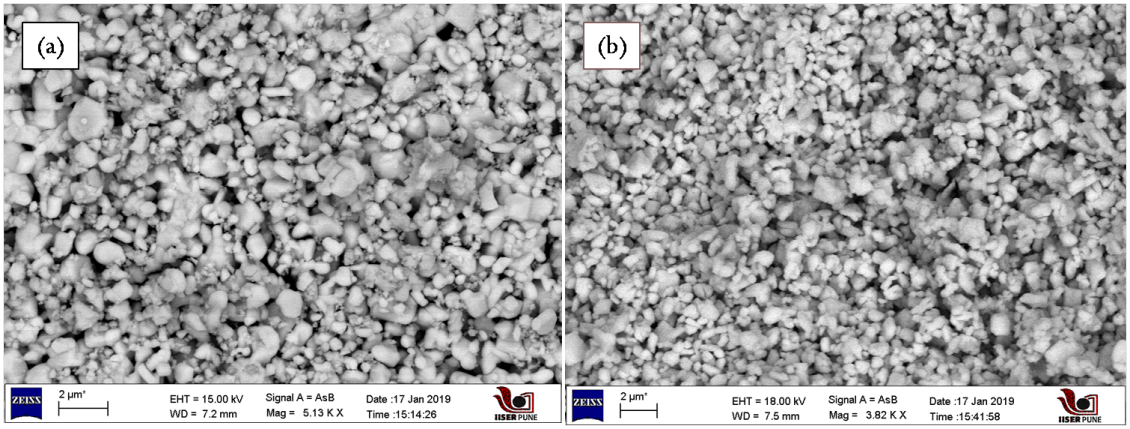

Figure 3.7: FESEM images for (a)Pr438 at 15 kV and (b)Nd438 at 18 kV.

FESEM Images of all the R438 (R = Nd, Pr) samples were also obtained (at 18 kV). EDS Spectrum was obtained at 11-12 points and the average R:Ni ratio turned out to be 1.38 and 1.42 for R = Pr and Nd respectively, slightly higher than the theoretical value of 1.33 expected for these samples. The grain size and shape are similar for the two samples.

3.3 Summary

From analysis of the X-ray diffraction patterns, we can say that we have successfully synthesized the R4310 sample using the sol-gel technique. For La4310, we had to switch from sintering in air (which was giving La327 phase) to sintering in oxygen atmosphere to obtain the La4310 phase. An attempt was also made to synthesize Ce-doped Pr4310 using this technique. But, as seen from the XRD plot, Ce was not substituting the Pr ion. Cell parameters were calculated using UnitCell[11] software and they follow the expected trend i.e., the cell parameters decrease with decreasing size of the rare earth ion. We were also able to successfully obtain R438 (R = Pr, Nd) by reducing the corresponding R4310 samples in 10% H_2-Ar atmosphere. Cell parameters were also calculated for these samples - they decrease with decreasing size of the rare earth ion. FESEM and EDS conducted on all these samples show a slightly enhanced R:Ni ratio.

Chapter 4

Thermogravimetric Analysis

In Chapter 2, a brief introduction to the technique of thermogravimetric analysis was given. As mentioned in Chapter 2, it is not possible to directly synthesize the R438 phases in the lab and they are obtained by reducing the corresponding R4310 phase. TG measurements were performed on the R4310 samples to ascertain the time and temperature combination for which the R438 phases are stable. In this chapter, we will summarize the results of the TG analysis on the R4310 samples.

For the R4310 series, the following reactions are expected to occur under a reducing (Ar + 10 % H_2) atmosphere :

1. $R_4Ni_3O_{10} + H_2 = R_4Ni_3O_9 + H_2O$
2. $R_4Ni_3O_{10} + 2H_2 = R_4Ni_3O_8 + 2H_2O$
3. $R_4Ni_3O_{10} + 4H_2 = 2R_2O_3 + 3Ni + 4H_2O$

4.1 La4310

La4310 showed a single weight loss step with a weight loss of ∼1.8% - this weight loss corresponds to the La439 phase and is within the error bar of our measurements. No step corresponding to the La438 phase was observed. A lower heating rate of 2.5 K/min was

employed in a subsequent experiment to see if the step corresponding to La438 could be resolved. An OTS (Oxygen Trapping System) was also used to remove traces of oxygen. However, no such step was obtained. This result is in conformity with previous reports where La438 phase is stabilized in pure H_2 flow only[2].

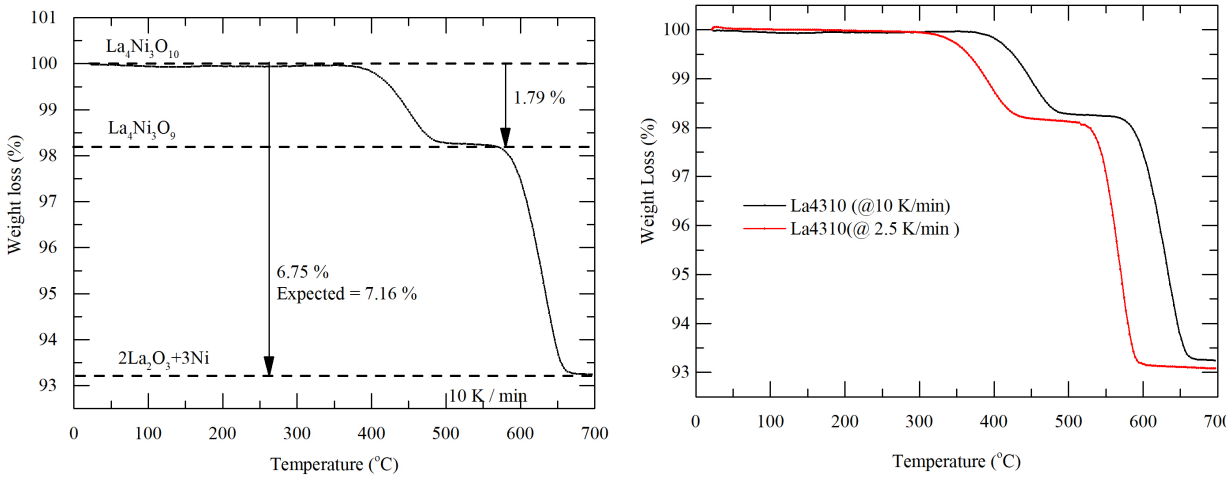

Figure 4.1: (a) Temperature scan for La4310 at 10K/min showing the various weight loss steps, (b) Comparison of temperature scans done at 10 K/min and 2.5 K/min - lower heating rate also did not resolve the step correspoding to La438.

4.2 Pr4310

For Pr4310, the temperature scan was performed at 10 K/min; and the step corresponding to Pr438 appeared around 550^oC. Surprisingly, for the Pr sample, no step corresponding to Pr439 could be observed. Isotherms at various temperatures were performed to obtain pure Pr438 which is stable for a long time. XRD analysis after each isotherm showed that : (i) complete decomposition into Pr_2O_3 and Ni occurred for the 620^oC (4 hours) isotherm; whereas, (ii) partial decomposition occurred for 520^oC (4 hours), 490^oC (4 hours) and 470^oC (5 hours) along with formation of Pr438 phase. For the 490^oC (45 mins) isotherm, the highest intensity peak of Pr4310 was observed. However, the isotherm performed at 500^oC for 1 hour gave pure Pr438 phase. The various isotherms are shown in Fig. 4.3(b). The XRD patterns of the decomposed products are shown in panel (c) of this figure.

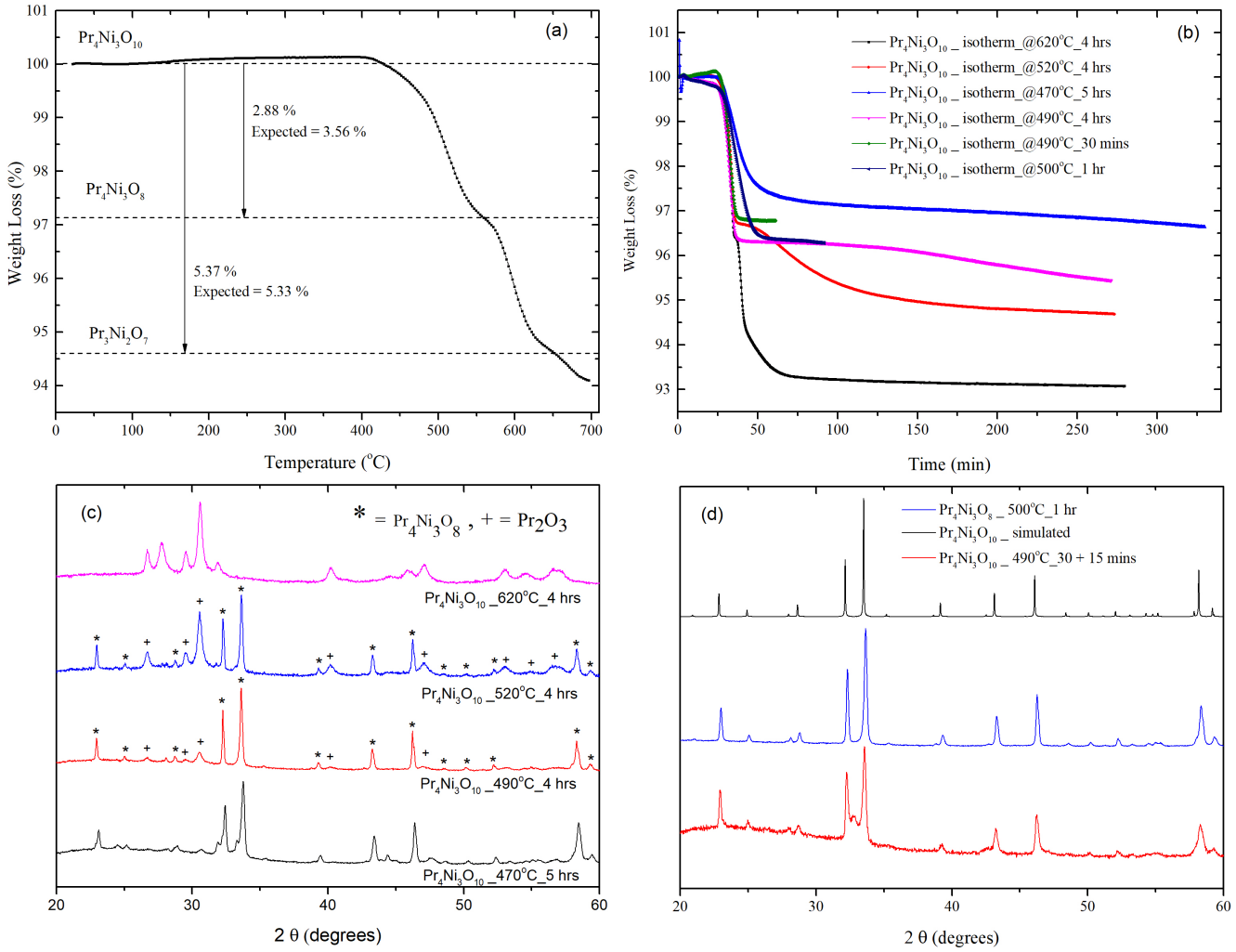

Figure 4.2: (a) Temperature scan for Pr4310 at 10K/min showing the various weight loss steps, (b) Isotherms done at various temperatures to obtain the conditions for which Pr438 phase is stable, (c) XRD done on powders subjected to isotherms at 620^oC (4 hours), 520^oC (4 hours), 490^oC (4 hours) and 470^oC (5 hours), and (d) XRD pattern of the powders subjected to isotherms at 490^oC (45 mins) and 500^oC (1 hour) - the 500^oC (1 hour) isotherm gives pure Pr438 as can be seen from comparison with the simulated pattern.

4.3 Nd4310

For Nd4310, the TGA steps were not well resolved at 10 K/min. To better resolve the steps, a temperature scan at 5 K/min was performed. Two steps were observed in the data (Fig. 4.3(a)) – the first with a weight loss of $\sim 1.7\%$ at around 485^oC which corresponds to the Nd439 phase; and, the second step at around 565^oC with a weight loss of $\sim 3.7\%$ which corresponds to the Nd438 phase. To stabilize the Nd438 phase, isotherms were performed at 540^oC for 2 hours and 470^oC for 3 hours and 30 minutes. XRD of the powder after the two isotherms showed that pure Nd438 was obtained at 470^oC as shown in panel (c) and (d) of Fig. 4.3.

4.4 Summary of TGA

We were successfully able to stabilize the R438 phase for R = Pr and Nd under 10% $H_2 - Ar$ but not the La438 phase for which probably pure H_2 atmosphere is required as reported previously. A new step corresponding to Nd439 phase which has not been reported previously, was observed in the TGA data. While steps corresponding to the R439 phase were observed only for R = La and Nd, it was not observed for R = Pr.

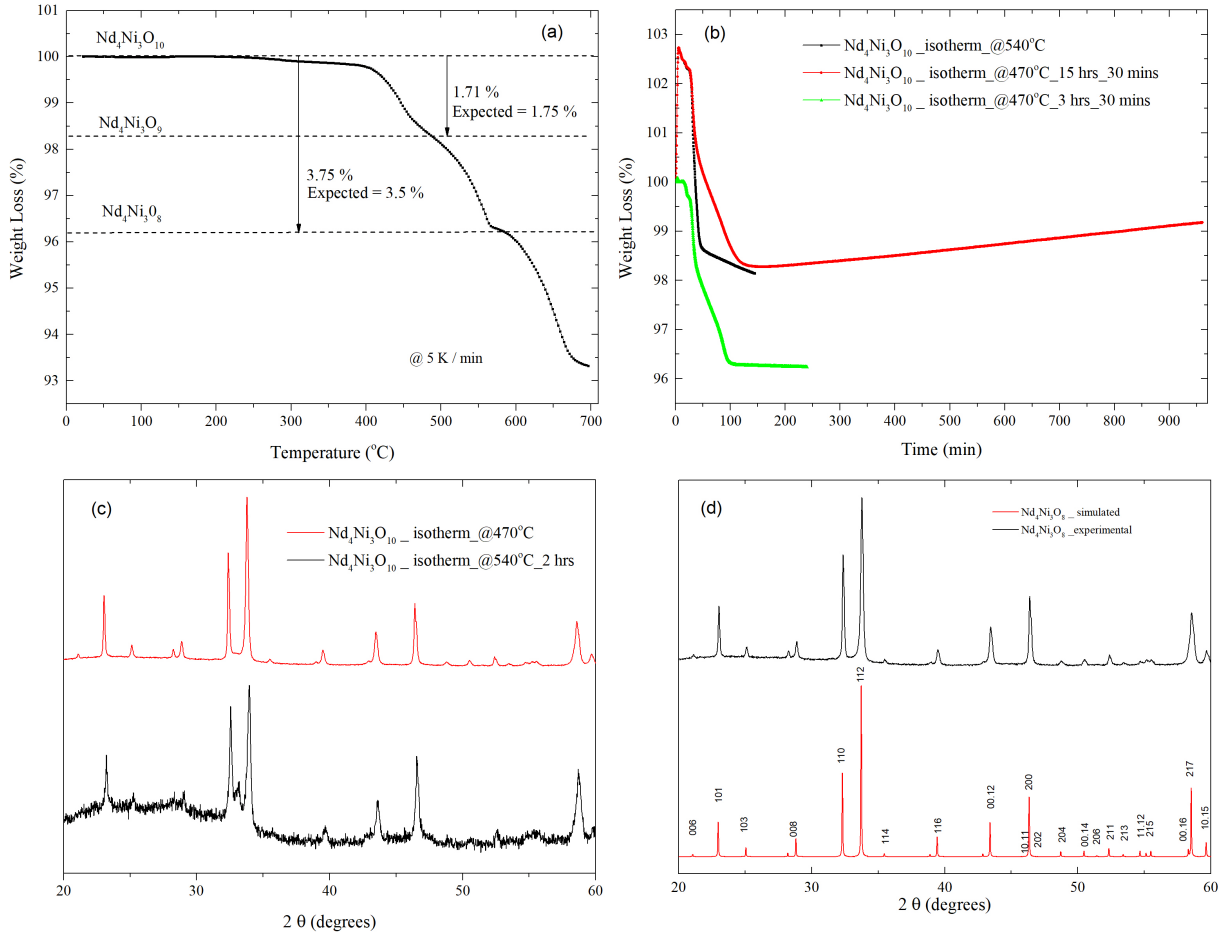

Figure 4.3: (a) Temperature scan for Nd4310 at 5K/min, (b) Isotherms at 540^oC and 470^oC, (c) XRD of the samples subjected to isotherms at 540^oC and 470^oC, and (d) Comparison of the XRD plot of the 470^oC isotherm with the simulated pattern of Nd438.

Chapter 5

Low temperature physical properties of $R_4Ni_3O_{10}$ (R=La, Pr and Nd)

This chapter deals with the low temperature physical properties measurement like resistivty, susceptibility, magnetisation and specific heat of the R4310 samples. Along with the reported anomalies in the resistivity data, we have also observed new features at low temperatures which have not been reported previously. In this chapter, we present the analysis that we have done to gain insight into the physics of these RP nickelates.

5.1 La4310

The ρ vs T plot for La4310 shows an anomaly at 136 K (Fig. 5.1(a)), which is in good agreement with previous reports[8] and has been attributed to a charge density wave (CDW) instability, although no experiments have been done to confirm this. Data was taken both during heating and cooling and the difference between the heating and cooling curves is within the error bar of the measurement. ρ(T) measured under a field of 5 T apllied perpendicular to the current flow did not show any measurable field dependence. In particular, no hysteresis was observed at the transition temperature which suggests that the anomaly is not due to a first order transition.

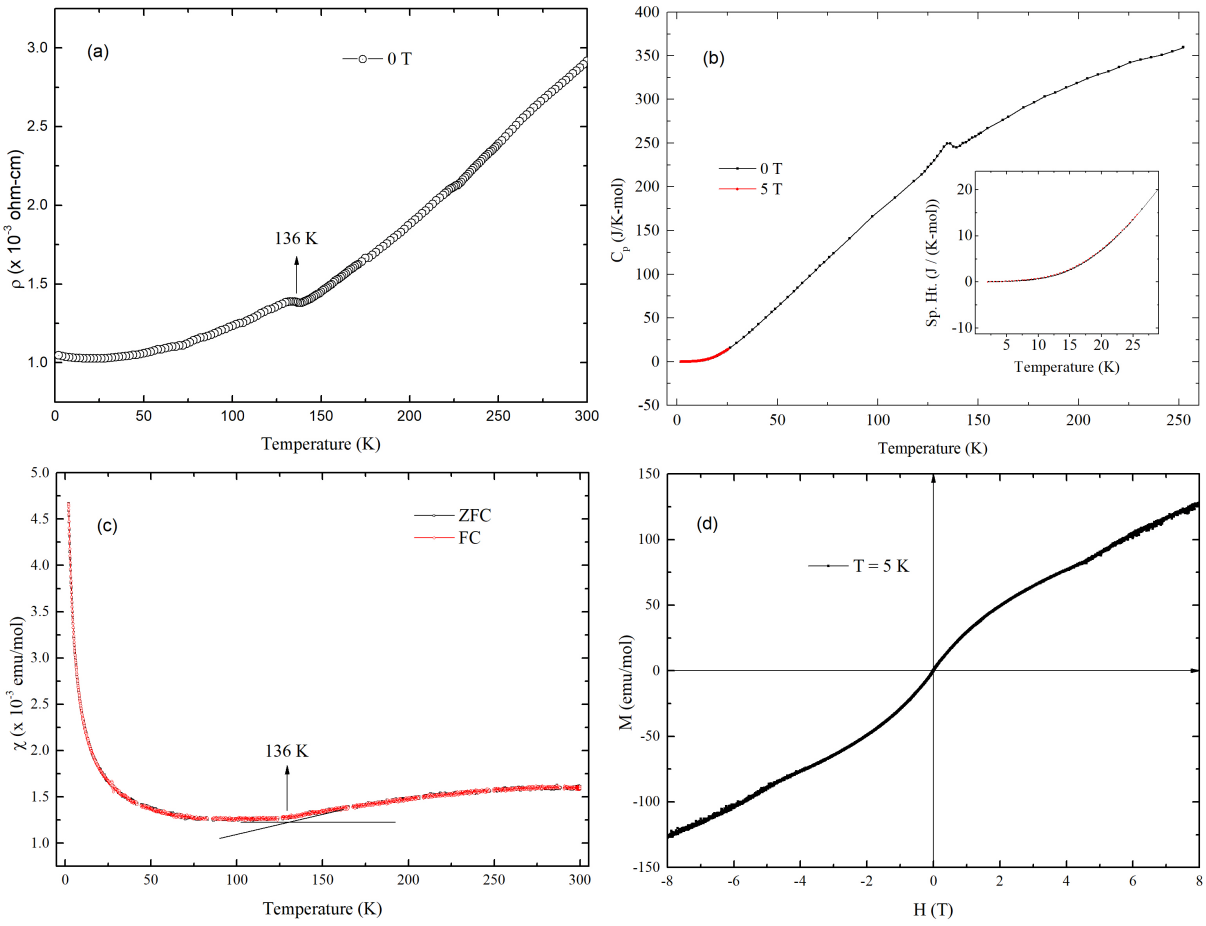

Figure 5.1: La4310 : (a) Resistivity data showing an anomaly at 136 K, (b) Specific heat showing a λ-shaped peak at 136 K, (c) Susceptibility data with a change in slope at 136 K, and (d) M vs H.

In La4310, La is in 3+ oxidation state and is therefore non-magnetic. Hence, the magnetic contribution in this compound comes only from the Ni sub-lattice. In the susceptibility data, a change of slope occurs at 136 K, which coincides with the resistivity anomaly. In the paramagnetic state, as the temperature decreases, one would expect thermal energy to decrease, and hence the spins should have an increased tendency to line up parallel to the applied magnetic field. This would lead to a rise in susceptibility with decreasing temperature. However, in the case of La4310, contrary to what one would expect, the susceptibility first decreases with decrease in temperature from 300 K down to 136 K and then starts to increase as the temperature is decreased further. This probably suggests that

the Ni spins order above room temperature. A Curie tail was fit to the χ vs T between T = 2 K and 10 K which gave $\chi_0 \sim 10^{-3}$ emu $mol^{-1}Oe^{-1}$, $C \sim 1.7 \times 10^{-2}$ emu K $mol^{-1}Oe^{-1}$ and $\theta_p \sim 2.7$ K. χ_0 is large and positive but one cannot attribute it to the Pauli paramagnetism of the free electrons which is typically two to three orders of magnitude smaller. The high value of χ_0 probably suggests that the sharp rise in χ at low temperatures is an intrinsic property of the sample. The M vs H curve also could not be fitted to the Brillouin Function which also rules out the presesnce of free spins.

The anomaly observed in the resistivity and susceptibility data also shows up as a peak at 136 K in the specific heat data. Since this peak remains unaffected by the application of a magnetic field of 5 T, we can conclude that the anomaly has a non-magnetic origin and may probably arise from the structural rearrangement associated with CDW ordering, which further strengthens the argument for a CDW instability. The low temperature $\frac{Cp}{T} vs T^2$ was fit to $\gamma + \beta T^2$, where γ is the electronic contribution and β is the phononic contribution. This fit yielded $\gamma \sim 5mJ/Ni - molK^2$ and $\beta \sim 0.5mJ/mol - K^4$. The γ value is slightly larger than that reported by Wu[12] for $La_4Ni_3O_{10}$ and is about an order of magnitude larger than that calculated for Cu by simple free electron theory ($\sim$ 0.5 mJ mol^{-1} K^{-1}). Such a large *gamma* value signifies strong electronic correlations. θ_D was calculated from β using the relation $\beta = \frac{12\pi^4 N k_B}{5\theta_D^3}$. This calculation gave $\theta_D \sim 400$ K.

5.2 Pr4310

Analogous to the case of La4310, the ρ vs T plot for Pr4310 also shows an anomaly at 156 K which has been previously attributed to a CDW instability[8]. Below 75 K, there is an upturn in the resistivity which has not been reported previously. As shown in the figure, the heating and cooling data overlap which suggests that there is no thermal hysteresis in the sample. The measurement of ρ under an applied magnetic field of 5 T overlapped with the zero-field data, suggesting that the magnetoresistance of the sample is very small. This suggests that the transition at 156 K is not first-order in nature.

The magnetic susceptibility (χ) data of Pr4310 is considerably more complicated because of the presence of two magnetic sub-lattices – the Pr sub-lattice and the Ni sub-lattice. The low temperature χ vs T data shows an anomaly between 5 K and 15 K (the derivative of the χ vs T plot in this range shows a change in slope and is highlighted in the inset of Fig. 5.2

(c)) which has not been reported previously[8]. χ vs T between 175 K to 285 K was fit to the Curie –Weiss law which gave $\chi_0 \sim 2.8 \times 10^{-3}\ emumol^{-1}Oe^{-1}$, C $\sim 6.3\ emuKmol^{-1}Oe^{-1}$ and $\theta_p \sim$ -36 K. The experimental effective magnetic moment per formula unit can be calculated from the Curie constant C using the formula $\mu_{eff} = \sqrt{8C}$ which turned out to be $\sim 7.2\mu_B$. Theoretically, μ_{eff} for Pr4310 will be given by $\sqrt{4\mu_{eff}|^2_{Pr} + 3\mu_{eff}|^2_{Ni}}$. Substituting the theoretical value of μ_{eff} for Pr^{3+} ion (which is $3.58\mu_B$) in the above equation gives a rather small (almost zero) magnetic contribution from the Ni sublattice. But we know that Ni in our sample is present as Ni^{3+} and Ni^{2+} in the ratio 2:1; and since both Ni^{3+} and Ni^{2+} are magnetically active (unless Ni^{2+} is in the low spin state), the $\mu_{eff}|_{Ni} = 0$ obtained from the CW fit is rather surprising. It is possible that the Ni moments in this temeperature range are magnetically ordered. This argument is supported by the susceptibility data of La4310 where the magnetic contibution comes only from the Ni moments and susceptibility decreases with decrease in temperature in the temperature range 175 K to 285 K. χ_o is positive and two orders of magnitude larger than that expected from Pauli paramagnetism of free spins. The θ_p value is in good agreement with that reported by Bassat et al.[13]. M vs H for this sample could also not be fit to a Brillouin function which rules out a paramagnetic ground state for the Pr moments. This is also in agreement with the value of θ_p which is significantly large and its negative sign suggests antiferromagnetic correlations between the Pr moments.

The C_p vs T plot for Pr4310 shows a λ-shaped peak at 156 K which coincides with the resistivity anomaly. The peak remains unaffected on application of magnetic field which once again indicates that the 156 K transition is not due to any magnetic ordering which would have shown some variation in response to the applied magnetic field. The possibility of a structural modulation accompanying the CDW ordering appears to be more likely. Also, as seen in Fig. 5.2(b), a hump is seen in the low temperature region (magnified in the inset) which does not change on application of magnetic field.

To analyze our specific heat data, we have followed the method adopted by Cheng et al[14] to analyse the specific heat data of $PrMnO_3$. Since La4310 and Pr4310 are isostructural, subtracting $(C_p/T)_{La4310}$ from the $(C_p/T)_{Pr4310}$ gives the contribution of the 4f electrons of Pr (Fig. 5.3) in the low temperature range (i.e., T«T_{CDW}), where the contribution to C_p due to the Ni sub-lattice can be assumed to be same for the two cases. From this analysis, we see that the contribution of the 4f electrons persists upto very high temperatures. This subtraction also reveals 2 peaks – one at $T_1 \sim 5$ K and the other at $T_2 \sim 36$ K (Fig. 5.3).

For estimating the entropy enclosed by the hump at low temperatures, $\frac{Cp}{T} vs T^2$ between 16 K and 24 K was fitted to $\gamma + \beta T^2$ and this background was subtracted from the $\frac{Cp}{T} vs T^2$ plot of Pr4310. The resulting curve showed a peak at around 5 K and the area under the curve (between 0 K to 17 K) gave the entropy S where $S = \int_0^T \frac{C_p}{T} dT$.

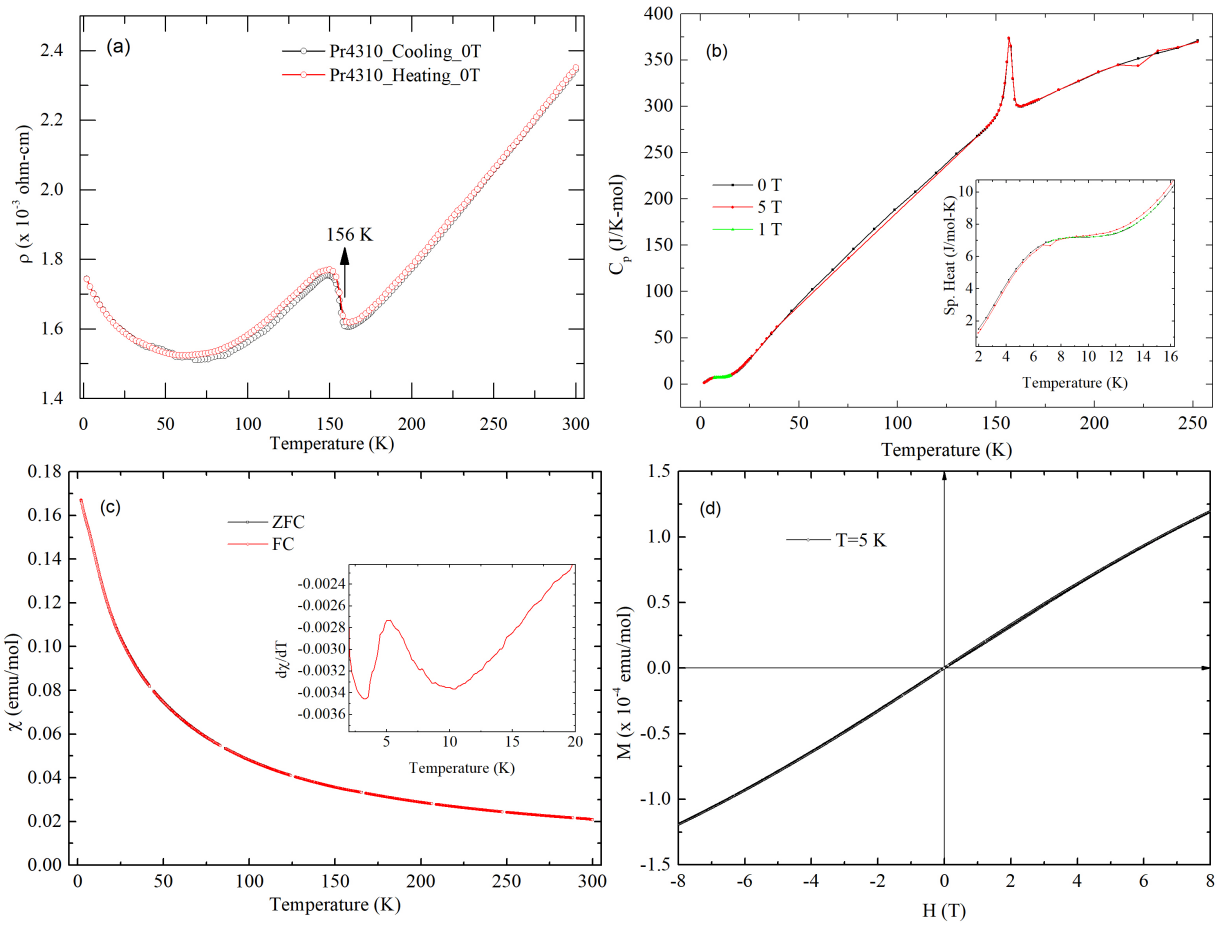

Figure 5.2: Pr4310: (a) Resistivity data with an anomaly at 156 K, (b) Specific heat with a λ-shaped peak at 156 K, (c) Susceptibility, and (d) M vs H.

S = 5.95 J/mol-K by this calculation. Thus the entropy per Pr-mole (S_{Pr}) is S/4 or 1.49 J Pr-mol^{-1}K^{-1}. This is about 26% of Rln2. Since one-fourth of the Pr atoms in Pr4310 reside in the rock-salt layer, it can be concluded that this hump at low temperatures arises because of the ordering of Pr^{3+} in the rock-salt layer, which is also manifested in the magnetic susceptibility in the form of an anomaly near T = 5 K, as shown in the inset of Fig.5.2(c).

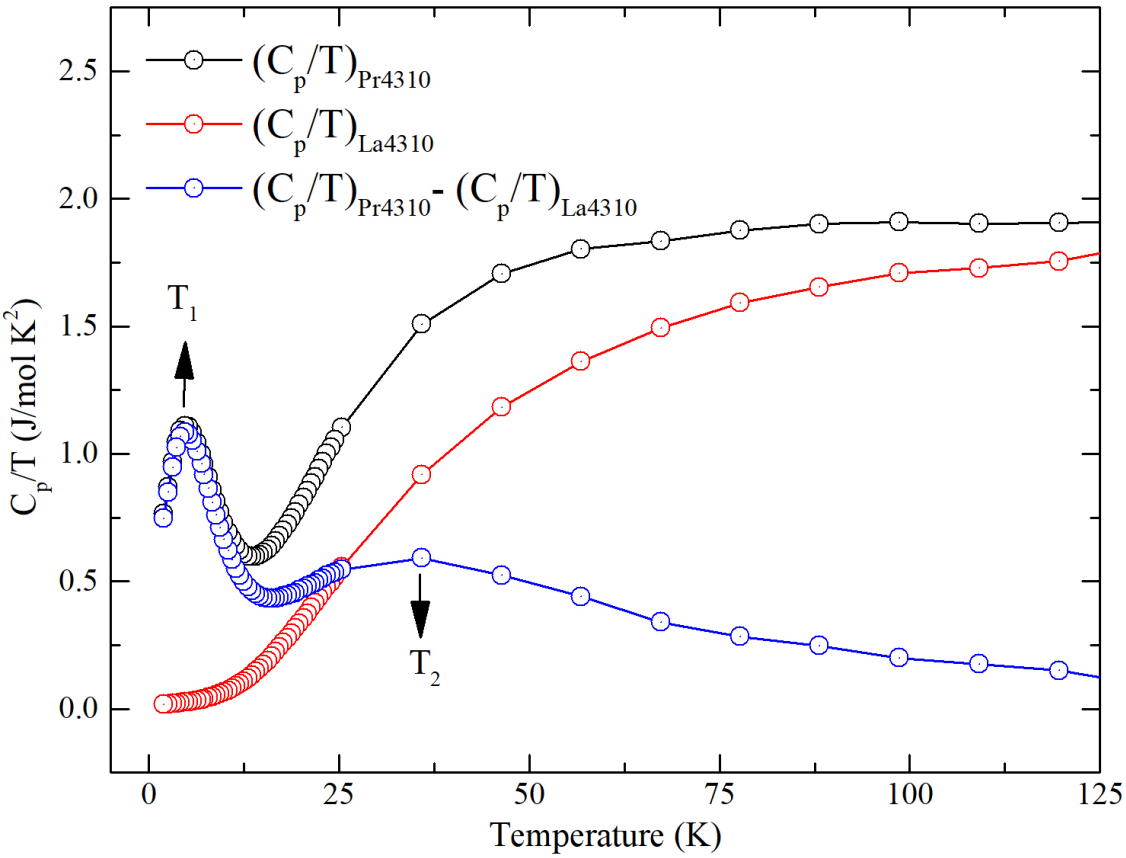

Figure 5.3: $\frac{C_p}{T}$ of La4310 (red curve) subtracted from that of Pr4310 (black curve) shows two humps (blue curve)- one at $T_1 \sim 5$K and the other at $T_2 \sim 36$ K.

In a previous inelastic neutron scattering study on $PrNiO_3$ by Rosenkranz et al[15], the 9 degenerate J-multiplets of the Pr^{3+} ion split into 9 singlets due to the crystalline electric field at the Pr site. The energy gap between the ground state singlet (E_0) and the first excited state singlet (E_1) is 6.4 meV which corresponds to T = 37 K. Since Pr4310 contains 3 perovskite $PrNiO_3$ layers, we can approximate, upto first order, that the splitting of the ground state J- multiplet of the Pr ions in the perovskite layers in Pr4310 is similar to that found in the infinite layer $PrNiO_3$. This assumption agrees quite well with the peak temperature T_2 of the second hump. Under an applied field of 5 T, the energy gap between E_0 and E_1 will change only marginally; therefore this feature is expected to have a very weak magnetic field dependence, in agreement with the experimental observation.

To summarize, from combined resistivity, specific heat and magnetisation study, we con-

clude that Pr^{3+} moments in the rock-salt layer of Pr4310 undergo magnetic ordering but the Pr^{3+} moments in the perovskite layers remain unordered down to 2K due to singlet nature of the crystalline electric field split lowest J-multiplet.

5.3 Nd4310

An anomaly, similar to that seen in La4310 and Pr4310, shows up in the resistivity measurement of Nd4310 at 160 K, which is in good agreement with previous reports and has been attributed to a CDW instability in this system[8]. However, unlike in reference[8], the resistivity goes on increasing below the transition. The upturn could be due to the presence of $NdNiO_3$ phase which shows a metal to insulator transition at 201 K[16]. However, this possibility is ruled out since no evidence of this phase is seen in the XRD pattern or the specific heat.

Just like in the case of Pr4310, Nd4310 also has two magnetic sub-lattices – the Nd sublattice and the Ni sub-lattice. χ vs T between 175 K and 285 K was fitted to the Curie-Weiss law which gave $\chi_0 \sim 3.8 \times 10^{-3}$ emu $mol^{-1}Oe^{-1}$, C$\sim$ 6.3 emu K $mol^{-1}Oe^{-1}$ and $\theta_p \sim$ -42 K, although no ordering is seen in the susceptibility data at this temperature. Using the equations defined for experimental and theoretical μ_{eff} in the previous section, we see that the magnetic contribution from the Ni sublattice is negligible. M vs H curve obtained at 5 K did not show any hysteresis and could not be fit to a Brillouin function. This rules out a paramagnetic ground state for the Nd ions.

The specific heat data also showed a λ-shaped peak which was concomitant with the resistivity anomaly at 160 K. Since the peak remained unchanged on application of magnetic field, we can conclude that the resistivity anomaly has a non-magnetic origin and is probably due to a structural transition. In the low temperature region, an upturn is observed in the zero field data which has not been reported in the previous studies[8]. On application of magnetic field, a hump appears which shifts towards higher temperatures as the magnetic field is increased. Such a behaviour is characteristic of a Schottky anomaly. For analysing this data, we first subtracted the background from the low temperature specific heat at 0 T (we have used the γ and β values of La4310 as a first approximation). Initially, we tried to

fit the resulting curve using a simple two level Schottky model :

$$C_{sch} = R(\frac{\Delta}{T})^2(g_0/g_1)\frac{\exp^{\Delta/T}}{(1+\exp^{\Delta/T})^2}$$

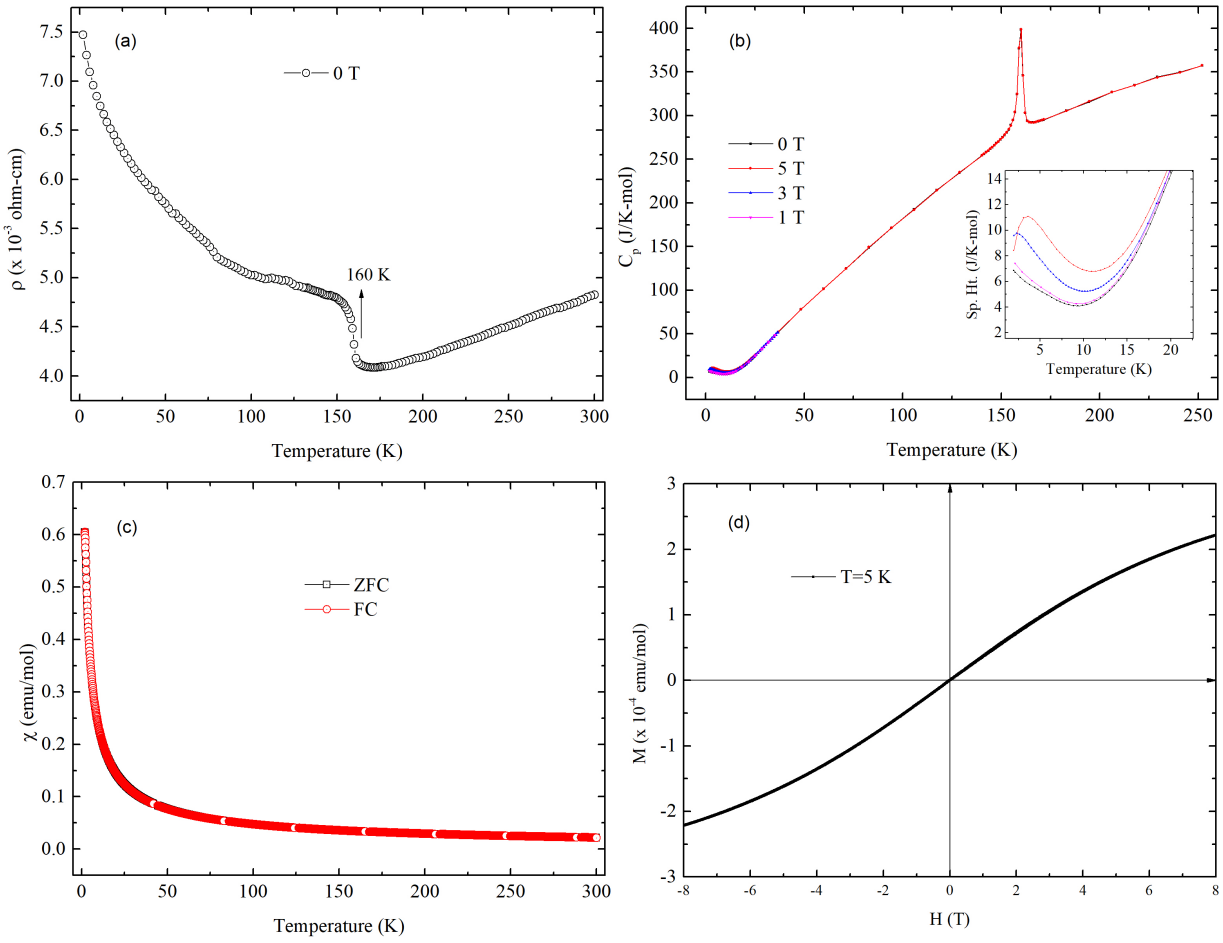

Figure 5.4: Nd4310: (a) Resistivity data showing an anomaly at 160 K, (b) Specific heat, showing a λ-shaped peak at 160 K, (c) Susceptibility and (d) M vs H.

where R is the universal gas constant, Δ is the energy difference between the two levels, g_o is the degeneracy of the ground state and g_1 is the degeneracy of the excited state. Since Nd^{3+} is a Kramer's ion (i.e., it has odd number of 'f' electrons), in the absence of a magnetic field, the minimum degeneracy of any state has to be two i.e. the 10-fold degenerate J-multiplet can split with following combinations for ground and first excited state crystal field split levels : g_o=2, g_1=2; g_o=2, g_1=4; g_o=4, g_1=2. Thus $g = \frac{g_o}{g_1}$ can be 0.5, 1 or 2. Data

were fitted using all of the above g values but we were unable to obtain a good fit in any of the three cases.

Since one-fourth of the Nd ions reside in the rock-salt layer and three-fourth of them reside in the perovskite layer, we tried fitting the data using a modified Schottky equation :

$$\frac{C_{sch}}{T} = R(\frac{\Delta_1^2}{T^3})(g_0/g_1)\frac{e^{\Delta_1/T}}{(1+e^{\Delta_1/T})^2} + 3R(\frac{\Delta_2^2}{T^3})(g_0/g_1)\frac{e^{\Delta_2/T}}{(1+e^{\Delta_2/T})^2}$$

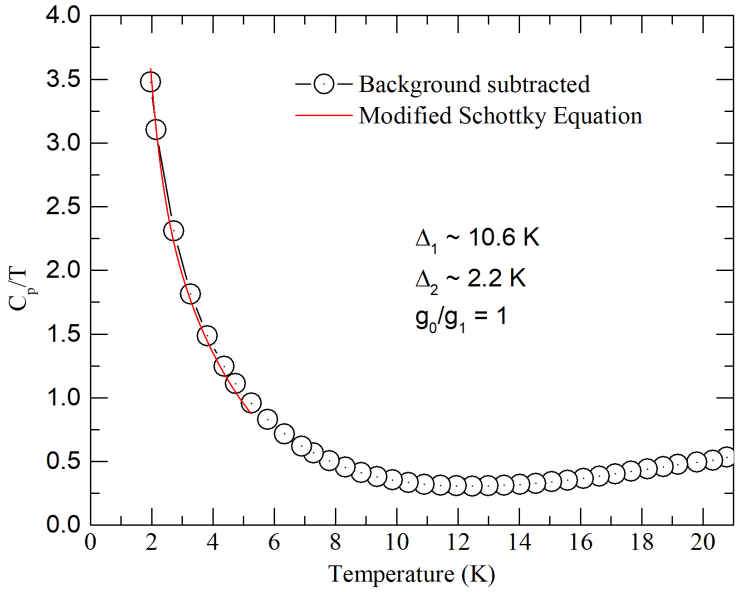

Figure 5.5: Modified Schottky equation fitted to background subtracted C_p/T of Nd4310

In a previous report on $NdNiO_3$[17], specific heat of the sample was measured in the low temperature region where a Schottky-type anomaly with a peak temperature at 1.7 K was observed which appears due to the splitting of the ground-state doublet due to the Nd-Ni exchange interaction. In the first order, we can approximate the perovskite layers in Nd4310 to behave as the infinite layer $NdNiO_3$ compound. Hence, we first fixed Δ_2 to be equal to 1.7 K and $\frac{g_0}{g_1}$ to be equal to 1 and varied Δ_1 keeping $\frac{g_0}{g_1}$=1 fixed for this term also (i.e., assuming that the ground state multiplet is a doublet). Then we varied Δ_2 as well and were able to obtain a reasonable fit between T = 2 K and 5 K with $\Delta_1 \sim 10.6$ K and $\Delta_2 \sim 2.2$ K which correspond to the splitting of the ground state doublet of the Nd ions in the rocksalt and perovskite layers respectively.

Chapter 6

Low Temperature Physical Properties of $R_4Ni_3O_8$ (R = Pr, Nd)

In this chapter, we will discuss the low temperature resistivity and specific heat data of the R438 samples and highlight the differences with the R4310 samples.

6.1 Pr438

Pellets obtained from two different reductions were used for measuring resistivity and specific heat. For the resistivity measurements, the pellet used had $\sim 3\%$ Pr_2O_3. The ρ vs T data are shown in Fig.6.1(a). These measurements revealed insulating behaviour of the sample. Data is shown only between 50 K to 300 K because the sample surpassed the compliance limit of the instrument below 50 K. Resistivity measurements of $Pr_4Ni_3O_{10}$ and $Pr_4Ni_3O_{8.25}$ by Bassat[13] showed that while Pr4310 is metallic, $Pr_4Ni_3O_{8.25}$ is insulating i.e. the sample turns insulating on decreasing the oxygen content. However, measurement of resitivity by Zhang et al[5] on single crystals of $Pr_4Ni_3O_8$ revealed metallic behaviour of the sample. Given that our resistivity measurements resemble those made by Bassat, perhaps we have made an off-stoichiometric sample i.e., $Pr_4Ni_3O_{8+\delta}$.

The specific heat behaviour of Pr438 is very different from that of Pr4310. Unlike Pr4310, specific heat measurements on Pr438 did not reveal any anomaly nor any hump in the low

temperature region, although C_p/T vs T^2 showed an anomaly at very low temperatures (highlighted in the inset of Fig.6.1(b)) which is yet to be analysed.

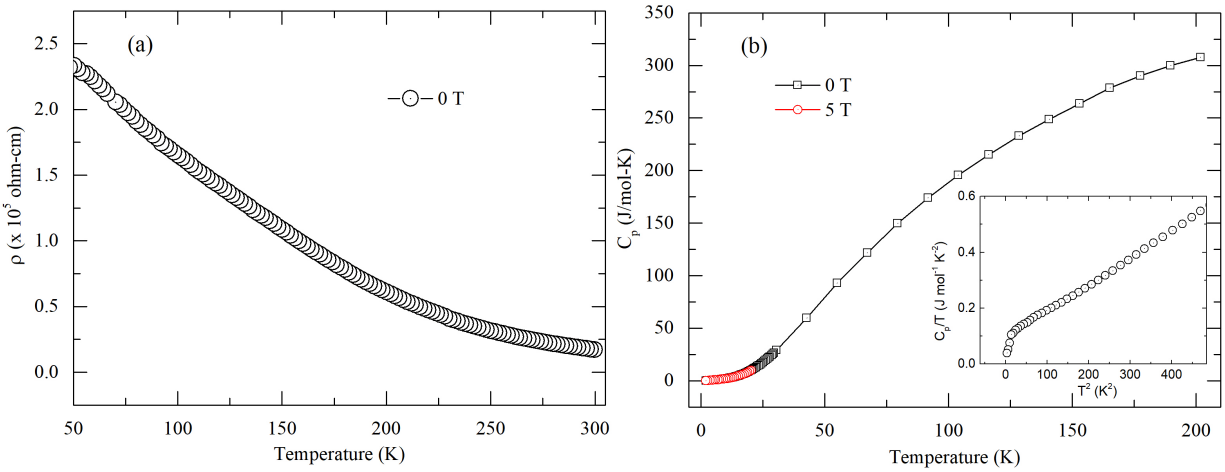

Figure 6.1: Pr438: (a) Resistivity, and (b) Specific heat.

6.2 Nd438

Resistivity and specific heat measurements were performed on the Nd438 samples. From the resistivity data (Fig. 6.2(a)), we can infer that the sample is insulating. The nature and magnitude of the resistivity is in agreement with previous reports[18]. Unlike in the case of Nd4310, the specific heat data (Fig. 6.2(b)) does not show any anomaly at higher temperatures. At low temperatures, there is an upturn in the data similar to that observed in the Nd4310 sample, which shifts towards higher temperatures on application of magnetic field. This behaviour is characteristic of a Schottky anomaly but the data are yet to be analysed.

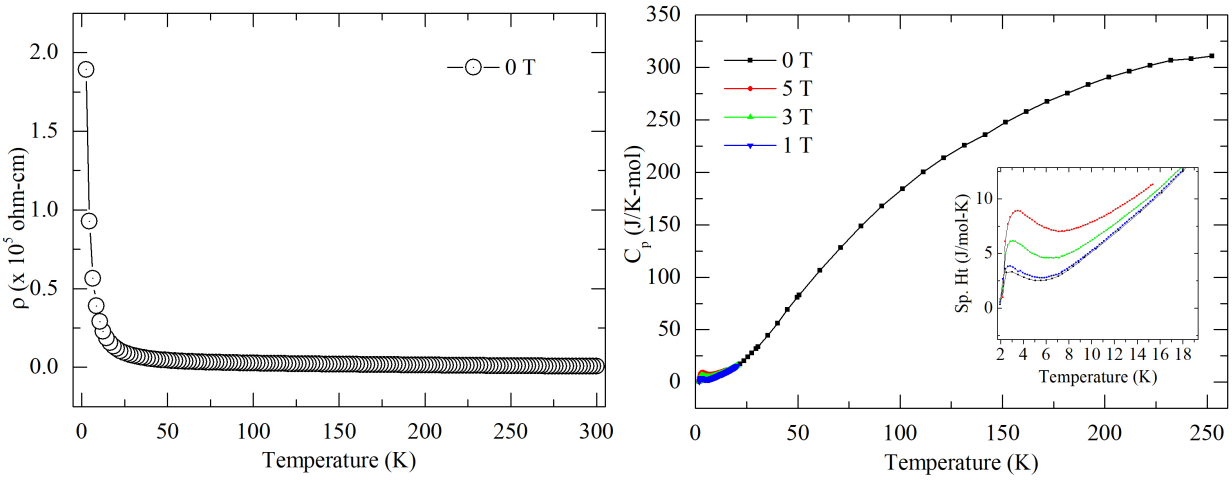

Figure 6.2: Nd438: (a) Resistivity, and (b) Specific heat.

Chapter 7

Conclusion

We have successfully synthesized the n=3 member of the Ruddlesden Popper phases with R=La, Pr and Nd using the sol-gel technique. The purity of the samples was confirmed through analysis of the XRD patterns. An attempt was also made to synthesize 5 % Ce-doped Pr4310 using the sol-gel technique which was unsuccessful. Thermogravimetric Analysis was employed to determine the temperature and time combination for which the corresponding R438 phases are stable. With 10%H_2-Ar atmosphere, we were only able to stabilize the Pr438 and Nd438 phases but not the La438 phase. From the TGA data, we have also found new steps corresponding to Nd439 phase which has not been reported previously. In the future, we plan to carry out topotactic reactions in order to stabilise the R438 phase, especially the La438 compound and study the low temperature properties of these systems in greater detail.

Physical properties of these samples were also measured between 2–300 K. Anomalies are observed in the resistivity data at 136 K, 156 K and 160 K for La4310, Pr4310 and Nd4310 respectively which is in good agreement with previous reports. Theoretical calculations have suggested that these anomalies are a result of CDW instability in these systems. For this, we plan to carry out low temperature XRD in the coming months. However, below the transition temperature, the resistivity measurements show deviations from those previously reported in literature. Further analysis is required to understand the origin of these anomalies.

For the La4310 sample, an anomaly is seen in the magnetisation data which is concurrent with the anomaly in the resistivity data. Also, the increase in susceptibility with increasing

temperature between 136 K and 300 K probably points towards ordering of Ni ions. VSM measurements above room temperature should be conducted in order to ascertain whether this is indeed the case. Fitting of susceptibility data to the Curie-Weiss law yielded large positive value of χ_o for all three samples. Also, the M vs H curve for all three samples could not be fitted to the Brillouin function. These results suggest that the ground state of these systems is not paramagnetic. Further analysis is required to better understand these data.

New features were also observed in the specific heat measurements of the Pr4310, Nd4310, Pr438 and Nd438 samples at low temperatures. In a first approximation, level splitting scheme of R^{3+} in $RNiO_3$ phase was used in order to understand the anomalies observed in R4310 (R=Pr, Nd) samples. For the Pr4310 sample, analysis of the specific heat data revealed 2 peaks - $T_1 \sim 5$ K which is probably due to the Pr ions residing in the rocksalt layer and $T_2 \sim 36$ K which is probably due to the Pr ions residing in the infinite perovskite layers. Initially, we attempted to fit the low temperature specific heat of Nd4310 using a simple 2-level Schottky equation - this, however, did not yield a good fit. So a modified Schottky equation was used to fit the zero field data. This equation gave reasonably good fitting parameters. However, the energy level splitting of the ground state doublet (Δ_1) of the Nd ions in the rocksalt layer in zero field seems to be unusually high. At present, we do not know the cause of this high Δ_1 value obtained from the fitting. Hence, we also plan to carry out inelastic neutron scattering measurements on these samples to determine the exact level splitting scheme.

Bibliography

[1] J George Bednorz and K Alex Müller. Possible hight c superconductivity in the ba- la-cu- o system. *Zeitschrift für Physik B Condensed Matter*, 64(2):189–193, 1986.

[2] Ph Lacorre. Passage from t-type to t′-type arrangement by reducing r4ni3o10 to r4ni3o8 (r= la, pr, nd). *Journal of Solid State Chemistry*, 97(2):495–500, 1992.

[3] Colin K Blakely, Shaun R Bruno, and Viktor V Poltavets. Low-temperature solvothermal approach to the synthesis of la4ni3o8 by topotactic oxygen deintercalation. *Inorganic chemistry*, 50(14):6696–6700, 2011.

[4] VI Anisimov, D Bukhvalov, and TM Rice. Electronic structure of possible nickelate analogs to the cuprates. *Physical Review B*, 59(12):7901, 1999.

[5] Junjie Zhang, AS Botana, JW Freeland, D Phelan, Hong Zheng, V Pardo, MR Norman, and JF Mitchell. Large orbital polarization in a metallic square-planar nickelate. *Nature Physics*, 13(9):864, 2017.

[6] Antia S Botana, Victor Pardo, and Michael R Norman. Electron doped layered nickelates: Spanning the phase diagram of the cuprates. *Physical Review Materials*, 1(2):021801, 2017.

[7] Haoxiang Li, Xiaoqing Zhou, Thomas Nummy, Junjie Zhang, Victor Pardo, Warren E Pickett, John F Mitchell, and Dan S Dessau. Fermiology and electron dynamics of trilayer nickelate la 4 ni 3 o 10. *Nature communications*, 8(1):704, 2017.

[8] Z Zhang and M Greenblatt. Synthesis, structure, and properties of ln4ni3o10-δ (ln= la, pr, and nd). *Journal of solid state chemistry*, 117(2):236–246, 1995.

[9] Danilo Puggioni and James M Rondinelli. Crystal structure stability and electronic properties of the layered nickelate la 4 ni 3 o 10. *Physical Review B*, 97(11):115116, 2018.

[10] MariaáDeus Carvalho, FernandaáMadalena A Costa, Isabeláda Silva Pereira, Jeaná-Marc Bassat, JeanáClaude Grenier, et al. New preparation method of la n+ 1 ni n o 3n+ 1–δ (n= 2, 3). *Journal of Materials Chemistry*, 7(10):2107–2111, 1997.

[11] TJB Holland and SAT Redfern. Unit cell refinement from powder diffraction data: the use of regression diagnostics. *Mineralogical Magazine*, 61(404):65–77, 1997.

[12] Guoqing Wu, JJ Neumeier, and MF Hundley. Magnetic susceptibility, heat capacity, and pressure dependence of the electrical resistivity of la 3 ni 2 o 7 and la 4 ni 3 o 10. *Physical Review B*, 63(24):245120, 2001.

[13] JM Bassat, C Allançon, P Odier, JP Loup, M Deus Carvalho, and A Wattiaux. Electronic properties of pr4ni3o10±δ. *European journal of solid state and inorganic chemistry*, 35(2):173–188, 1998.

[14] JG Cheng, Y Sui, XJ Wang, ZG Liu, JP Miao, XQ Huang, Z Lü, ZN Qian, and WH Su. Specific heat of single-crystal prmno3. *Journal of Physics: Condensed Matter*, 17(37):5869, 2005.

[15] S Rosenkranz, M Medarde, F Fauth, J Mesot, M Zolliker, A Furrer, U Staub, P Lacorre, R Osborn, RS Eccleston, et al. Crystalline electric field of the rare-earth nickelates r nio 3 (r= pr, nd, sm, eu, and pr 1- x la x, 0<˜ x<˜ 0. 7) determined by inelastic neutron scattering. *Physical Review B*, 60(21):14857, 1999.

[16] Ph Lacorre, JB Torrance, JSAI Pannetier, AI Nazzal, PW Wang, and TC Huang. Synthesis, crystal structure, and properties of metallic prnio3: Comparison with metallic ndnio3 and semiconducting smnio3. *Journal of Solid State Chemistry*, 91(2):225–237, 1991.

[17] F Bartolome, MD Kuz'min, J Bartolome, J Blasco, J Garcia, and F Sapina. Low-temperature specific heat of ndmo3 (m= co, fe, cr, ni): magnetic ordering of nd. *Solid state communications*, 91(3):177–182, 1994.

[18] Yoshiki Sakurai, Narihiko Chiba, Yoshihide Kimishima, and Masatomo Uehara. Electronic and magnetic properties of la4ni3- xcuxo8 and nd4- ysmyni3o8. *Physica C: Superconductivity*, 487:27–30, 2013.